A&A, 699, A114 (2025)
https://doi.org/10.1051/0004-6361/202451513


Astronomy & Astrophysics

# The nature of the X-ray binary transient MAXI J1834–021: Clues from its first observed outburst

A. Manca[1,⋆], A. Marino[2,3,4], A. Borghese[5,6,7,8], F. Coti Zelati[2,3,9], G. Mastroserio[10], A. Sanna[1], J. Homan[11], R. M. T. Connors[12], M. Del Santo[4], M. Armas Padilla[5,6], T. Muñoz-Darias[5,6], T. Di Salvo[13], N. Rea[2,3], J. A. García[14,15], A. Riggio[1,16], M. C. Baglio[9], and L. Burderi[1,4]

[1] Università degli Studi di Cagliari, Dipartimento di Fisica, SP Monserrato-Sestu km 0.7, I-09042 Monserrato, Italy
[2] Institute of Space Sciences (ICE, CSIC), Campus UAB, Carrer de Can Magrans s/n, E-08193 Barcelona, Spain
[3] Institut d'Estudis Espacials de Catalunya (IEEC), E-08034 Barcelona, Spain
[4] INAF/IASF Palermo, via Ugo La Malfa 153, I-90146 Palermo, Italy
[5] Instituto de Astrofísica de Canarias (IAC), Vía Láctea s/n, La Laguna 38205, S/C de Tenerife, Spain
[6] Departamento de Astrofísica, Universidad de La Laguna, La Laguna E-38205, S/C de Tenerife, Spain
[7] INAF-Osservatorio Astronomico di Roma, Via Frascati 33, I-00040 Monte Porzio Catone (RM), Italy
[8] European Space Agency (ESA), European Space Astronomy Center (ESAC), Camino Bajo del Castillo s/n, 28692 Villafranca del Castillo, Madrid, Spain
[9] INAF, Osservatorio Astronomico di Brera, via E. Bianchi 46, I-23807 Merate (LC), Italy
[10] Dipartimento di Fisica, Università Degli Studi di Milano, Via Celoria 16, 20133 Milano, Italy
[11] Eureka Scientific, Inc., 2452 Delmer Street, Oakland, CA 94602, USA
[12] Department of Physics, Villanova University, 800 Lancaster Avenue, Villanova, PA 19085, USA
[13] Università degli Studi di Palermo, Dipartimento di Fisica e Chimica – Emilio Segrè, via Archirafi 36, I-90123 Palermo, Italy
[14] X-ray Astrophysics Laboratory, NASA Goddard Space Flight Center, Greenbelt, MD 20771, USA
[15] Cahill Center for Astronomy and Astrophysics, California Institute of Technology, Pasadena, CA 91125, USA
[16] INFN, Sezione di Cagliari, Cittadella Universitaria, 09042 Monserrato, CA, Italy

Received 15 July 2024 / Accepted 26 May 2025

**ABSTRACT**

MAXI J1834–021 is a new X-ray transient discovered in February 2023. We analysed the spectral and timing properties of MAXI J1834–021 using *NICER*, *NuSTAR* and *Swift* data collected between March and October 2023. The light curve showed a main peak followed by a second activity phase. Most of the spectra extracted from individual *NICER* observations could be adequately fit with a Comptonisation component alone, while some required an additional thermal component. The spectral evolution is consistent with a softening trend as the source becomes brighter in X-rays. We also analysed the broadband spectrum by combining data from simultaneous *NICER* and *NuSTAR* observations on March 10, 2023. This spectrum can be fitted with a disc component having an inner radius temperature of $kT_{\rm in} \sim 0.4$ keV and a Comptonisation component with a power-law photon index of $\Gamma \sim 1.8$. By including a reflection component in the modelling, we obtained a $3\sigma$ upper limit for the inner disc radius of 11.4 gravitational radii. We also detected a quasi-periodic oscillation (QPO), whose central frequency varies with time (from 2 Hz to ~0.9 Hz), and anti-correlates with the hardness ratio. Based on the observed spectral-timing properties, MAXI J1834–021 can be classified as a low-mass X-ray binary in outburst. However, we cannot draw a definitive conclusion about the nature of the accreting compact object, which could currently be a black hole or a neutron star.

**Key words.** accretion, accretion disks – binaries: general – stars: black holes – stars: low-mass – X-rays: individuals: MAXI J1834–021

## 1. Introduction

X-ray binary systems are roughly classified into two major subclasses: low-mass X-ray binaries (LMXBs; Chelovekov & Grebenev 2010; Bahramian & Degenaar 2023; Di Salvo et al. 2022), where the mass of the companion star is $\lesssim 1\,M_\odot$ (Lewin & Clark 1980), and high-mass X-ray binaries (HMXBs) where the companion star mass is $\geq 8\,M_\odot$ (Fortin et al. 2023). The two classes also differ in their accretion mechanisms. In LMXBs, accretion occurs through Roche-lobe overflow, when the companion star fills its Roche lobe and matter is pulled towards the compact object, forming an accretion disc. In HMXBs, accretion mainly occurs directly through the stellar wind of the companion star (see Karino et al. 2019, and references therein). The compact object can be either a black hole (BH) or a neutron star (NS). The presence of an NS can be inferred by the detection of peculiar features arising from the existence of a solid surface, such as type-I X-ray bursts – uncontrolled burning of fuel on the NS surface (see, e.g., Galloway & Keek 2021, for a review) – or X-ray pulsations (see, e.g., Di Salvo & Sanna 2022). However, the absence of these features does not necessarily imply the presence of a BH.

The population of LMXBs can be classified into persistent and transient systems. Persistent systems are characterised by a steady accretion rate and emit stable X-ray emission, sometimes with slight variations in intensity. In contrast, transient systems go through cycles of low activity (quiescence)

⋆ Corresponding author: arianna.manca@inaf.it

and high activity (outbursts). During quiescence, the X-ray luminosity drops below $10^{33}$ erg s$^{-1}$. However, during sudden outbursts, the luminosity can reach values of $10^{36-38}$ erg s$^{-1}$ (see Belloni & Motta 2016; Motta et al. 2021, for reviews on BH LMXBs, and see Di Salvo et al. 2022, for a review on NS LMXBs). The difference between persistent and transient sources could be due to either the timescale of these transitions – which might be too long to observe in persistent sources – or the mass accretion rate, which remains stable enough in persistent systems to support continuous X-ray emission, while it varies significantly in transient systems, leading to intermittent activity (see, e.g., Degenaar et al. 2014, 2017, and references therein for examples).

The spectral and timing properties of LMXBs enable the identification of various accretion states. These properties are studied through energy spectra, power density spectra (PDS), and hardness-intensity diagrams (HIDs). The energy spectra show two main components: a thermal multicolour disc and a Comptonised component that is usually modelled by a power law with a high-energy cutoff. In the case of NS LMXBs, an additional black-body-like component may emerge, caused by thermal emission from the NS solid surface or a boundary layer between the disc and the NS. The spectra of both BH and NS binaries can also show an Fe K$\alpha$ emission line at ∼6.4−6.7 keV, sometimes relativistically broadened, due to fluorescence or recombination processes in the inner disc. A reflection hump can appear at energies ∼ 20 keV (see Fabian et al. 1989; Bhattacharyya & Strohmayer 2007; Cackett et al. 2008, for more details and examples of NS systems).

The states of BH LMXBs can be roughly identified according to their position in the HID. The outburst begins with the source leaving the quiescence state and entering a low luminosity/hard state (LHS). This state is characterised by a predominance of the Comptonisation component. As the spectrum softens, the source enters a hard-intermediate state (HIMS), where the thermal component emerges and the hard power-law component becomes steeper. The HIMS is followed by the soft-intermediate state (SIMS) moving farther to the left of the HID, in which the spectrum becomes slightly softer. In the high-luminosity soft state (HSS), the spectrum becomes dominated by the thermal accretion disc component, which peaks at temperatures of ∼1 keV. By the end of the outburst, the source re-enters the HIMS at lower luminosities than during the hard-to-soft transition, then returns to the LHS again and reaches quiescence. This hysteresis cycle was first reported by Miyamoto et al. (1995) for BH candidate LMXBs. The relationship between X-ray luminosity and state transitions is not straightforward, as different systems reach the same X-ray luminosity in different spectral states; therefore, the X-ray luminosity at the transition is not identical for all sources. Some sources do not complete the transition to soft states. These 'failed-transition' outbursts are divided into two groups: the outbursts in which the source transitions to the HIMS, but never reaches the HSS; and those in which the source does not transition to the HIMS, but peaks in the LHS (Alabarta et al. 2021). Failed-transition outbursts have been observed in both BH (Capitanio et al. 2009; Del Santo et al. 2016; Bassi et al. 2019; García et al. 2019; Wang et al. 2022) and NS (see, e.g., Marino et al. 2022; Manca et al. 2023a,b) systems. In transient BH binaries, these outbursts are often referred to as 'hard-only' or 'failed-transition' outburst and are observed in about 40% of sources in this class (Alabarta et al. 2021). These outbursts are generally fainter than those featuring complete hard-to-soft transitions (Tetarenko et al. 2016). Although still not fully understood, the 'failed state transition' behaviour is thought to result from the mass accretion rate not reaching a specific threshold (see, e.g., Esin et al. 1997; Marcel et al. 2022), suggested to be about 0.1 $L_{\rm Edd}$ (Tetarenko et al. 2016), where $L_{\rm Edd}$ is the Eddington luminosity for a stellar-mass BH, or alternatively from the mass distribution in the accretion disc (Campana et al. 2013). Quasi-periodic oscillations (QPOs) can appear in the PDS in different spectral states as narrow, discrete features. They have been hypothesised to be related to characteristic periodicities of the accretion flow, such as the Keplerian motion of matter in the disc and the precession motions (see, e.g., Ingram et al. 2009; Ingram & Motta 2014, for one possible interpretation). These oscillations are usually divided into high-frequency QPOs and low-frequency QPOs, with the latter further classified as Type-A, B, and C (Wijnands et al. 1999; Remillard et al. 2002; see Ingram & Motta 2019, for a review). Type-C QPOs are observed in the HIMS and LHS, while Type-B and Type-A are only seen during the transition to the soft state.

Neutron star LMXBs exhibit spectral properties similar to those of BHs, but with some differences due to the presence of a surface. These NS LMXBs are generally classified into two categories: Z sources and atoll sources. This classification is based on the track that the source follows in a colour-colour diagram (CCD) during an outburst, as well as on its timing features (van der Klis 1989). Z sources typically have high mass accretion rates and correspondingly high luminosities, ≥0.5 $L_{\rm Edd}$. Atoll sources, have lower luminosities, 0.01−0.5 $L_{\rm Edd}$ (Lewin & van der Klis 2006). Therefore, this classification likely arises from differences in accretion rates, even though the underlying processes are similar (see e.g. Homan et al. 2010). For Z sources, the CCD is divided into three branches: the horizontal, normal, and flaring branch. During the activity phase, the source moves continuously along the Z-shaped track in the CCD. Atoll source states are classified into island, lower, and upper banana states. Outbursts in atoll sources evolve from the hard island states to the banana branch (see, e.g., Altamirano et al. 2008). Neutron star systems show a more diverse QPO phenomenology, and their classification is more complex.

In Z sources, low-frequency QPOs are classified into three main types: horizontal, normal, and flaring branch oscillations. These oscillations are believed to correspond to Type-C, B, and A QPOs of BHs, respectively (Casella et al. 2005). The same classification can be applied to atoll systems, which display only horizontal and flaring branch oscillation-like QPOs (Motta et al. 2017). Low-frequency QPOs may appear in low and intermediate states (see van der Klis 2006, for a full review).

A hysteresis-like spectral evolution is also observed in NS LMXBs in persistent and transient atoll sources (see Muñoz-Darias et al. 2014). The duration of this cycle generally matches the length of the outburst (∼1 month–year). However, in persistent sources or transients with long outbursts, multiple cycles can occur in succession. Similarly to BH LMXBs, in the HID, this cycle progresses in an anticlockwise direction, with the transition from hard to soft states occurring at the point of highest luminosity.

MAXI J1834–021 is an X-ray binary whose exact classification is still the subject of debate. The source was first detected on February 5, 2023 (MJD 59980) by MAXI/GSC (Negoro et al. 2023) as a new X-ray transient. The 2–10 keV X-ray flux was observed to increase during the outburst for a period of 10–20 days before decreasing again (Marino et al. 2023). No radio counterpart was found in Arcminute Microkelvin Imager Large-Array (AMI-LA) observations performed at a central frequency of 15.5 GHz (Bright et al. 2023).

In this work, we analyse the 2023 outburst of MAXI J1834–021 using *NICER*, *NuSTAR*, and *Swift* data. We outline the spectral properties of the outburst by individually analysing the *NICER* and *Swift* observations, and we analyse a broadband *NICER* and *NuSTAR* spectrum to investigate the presence of a reflection component. In addition, we conducted a timing analysis of the observations *NICER* and *NuSTAR* to determine the temporal variability and investigate a possible QPO component.

## 2. Observations and data reduction

MAXI J1834–021 was monitored from March 6 to October 2, 2023, with the Neutron Star Interior Composition Explorer (*NICER*; Gendreau et al. 2016) for a total exposure of 142 ks, divided into 81 observations, and with the *Swift* X-Ray Telescope (XRT) for a total exposure time of ∼73 ks, divided into 42 observations. In addition, the Nuclear Spectroscopic Telescope Array (*NuSTAR*; Harrison et al. 2013) observed the source on March 10, 2023 with an elapsed time of ∼55 ks and an on-source exposure time of ∼29 ks. Table A.1 lists the observations analysed in this work, including their respective start and stop dates, exposures, and source count rates.

Data reduction was performed using tools incorporated in HEASOFT 6.31. In the following, all uncertainties are quoted at the 90% confidence level (c.l.) unless otherwise stated.

### 2.1. NICER

*NICER* data were processed with the `nicerl2` pipeline, with default screening settings: (i) exclusion of time intervals in the proximity of the South Atlantic Anomaly; (ii) elevation angle of at least 30° over the Earth's limb; (iii) minimum angle of 40° from the bright Earth limb; and (iv) maximum angular distance between the source direction and *NICER* pointing direction of 0.015°. Visual inspection of several *NICER* light curves revealed irregular increases in count rates throughout the outburst. We determined that each of these corresponds to overshoots reaching values outside the recommended range, probably due to charged-particle contamination[1]. We decided to exclude the contaminated sections of the observations. We produced the spectra and background files with the `nicerl3-spect` pipeline, using the SCORPEON default model for the creation of the background file. We rebinned the data with FTGROUPPHA following the Kaastra & Bleeker optimal binning algorithm (Kaastra & Bleeker 2016) to ensure at least 20 counts per bin.

### 2.2. NuSTAR

*NuSTAR* data were processed and analysed using the NuSTAR Data Analysis Software (`nustardas`) and `caldb` v.20230404. The `nupipeline` tool was used with default options to create cleaned event files and filter out time intervals associated with the satellite passing through the South Atlantic Anomaly. For both focal plane modules (FPMs), source photons were collected within a circle of radius 90 arcsec centred on the source position, while background photons were extracted from a circle of radius 180 arcsec far from the source. MAXI J1834–021 was detected up to an energy of ≈60 keV in both FPMs. Background-subtracted spectra, instrumental responses, and auxiliary files were created using the `nuproducts` tool. The spectra of both FPMs were grouped to have at least 100 counts per energy channel.

### 2.3. Swift

The *Swift* single exposure ranged from 0.2 to 3.4 ks, with the XRT operating either in windowed timing (WT; readout time of 1.77 ms) or photon counting (PC; 2.51 s) modes. We processed the data adopting standard cleaning criteria and created exposure maps with the `xrtpipeline` task. For spectral analysis, we selected events with grades 0–12 and 0 for PC and WT data, respectively. We accumulated the source counts from a circular region with a radius of 20 pixels (1 pixel = 2.36 arcsec). To evaluate the background, we extracted the events within an annulus centred on the source position with radii of 40–80 pixels and 80–120 pixels for PC mode and WT mode observations, respectively. For PC mode pointings affected by pile-up, we followed the online analysis thread[2] to determine the size of the core of the point-spread function to be excluded from our analysis. We generated the spectra with the corresponding ancillary response files through `xselect` and the `xrtmkarf` tool. The response matrices versions 20131212v015 and 20130101v014 available in the XRT calibration database were assigned to each spectrum in WT and PC mode, respectively. The *Swift*-XRT background-subtracted spectra were grouped according to a variable minimum number of counts depending on the available counting statistics, varying between 10 and 40 counts per spectral bin.

## 3. Data analysis and results

### 3.1. Source position

We calculated the XRT position of MAXI J1834–021 using the *Swift* UK Swift Science Data Centre's online tool[3] with the UltraViolet and Optical Telescope-enhanced method (Evans et al. 2009). We derived right ascension (RA) = $18^{h}36^{m}09\overset{s}{.}09$, declination (Dec) = –02°17′15.″6 (J2000.0), with an error radius of 2.4″ at the 90% confidence level. This updated position does not coincide with any optical source listed in Gaia DR3 (Gavras et al. 2023), nor with the two optical sources detected in prompt observations by the Las Cumbres Observatory and Faulkes (Saikia et al. 2023) at a 90% c.l. The closest optical source, a faint object with a magnitude *G* of 20.8, is 2.5 arcsec away, and thus only marginally consistent with this position.

### 3.2. Outburst light curve and hardness intensity diagram

The left panel of Figure 1 presents the light curve of the outburst extracted using data from *NICER* and *Swift*. The outburst displays a complex morphology, beginning with its peak, followed by an approximately 100-day-long decrease, and then a rebrightening phase of similar duration. The highest count rate recorded by *NICER* is ∼30 cts s$^{-1}$ on MJD 60014, followed by a decrease to the level of ∼5 cts s$^{-1}$ and a subsequent rise to ∼20 cts s$^{-1}$. The level remains almost constant between 10 and 20 cts s$^{-1}$ for about two to three months, slowly decreasing to ∼10 cts s$^{-1}$ around October 2, 2023, the end date of the observations. No type-I bursts are detected in our data. As shown in the right panel of Fig. 1, we also derive the hardness ratio, with the soft band defined as the range 0.5–3 keV and the hard band as

[1] https://heasarc.gsfc.nasa.gov/docs/nicer/analysis_threads/overshoot-intro/

[2] https://www.swift.ac.uk/analysis/xrt/pileup.php

[3] https://www.swift.ac.uk/user_objects/

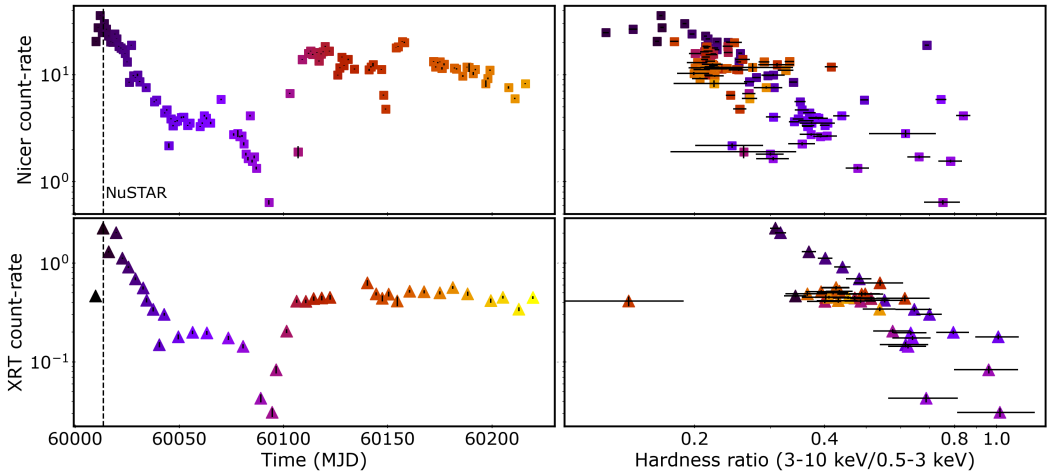


**Fig. 1.** Light curve (left panel) and HID (right panel) extracted from *NICER* (top) and *Swift*-XRT (bottom). Count rates were calculated in the 0.5–10 keV energy range, while hardness ratios were derived considering the 0.5–3 and 3–10 keV energy bands for both instruments. The colour gradient indicates the temporal sequence. Vertical dashed lines in the left panels denote the epoch of the *NuSTAR* observation.

3–10 keV. In the HID, most observations stack at similar hardness ratio values, e.g., at ∼0.2–0.4 for *NICER*, for varying count rates. Only observations taken when the source was at its lowest luminosity significantly deviate from the above trend, exhibiting an increase in hardness.

### 3.3. Spectral analysis

For all instruments, we performed the spectral analysis within XSPEC 12.13.1 (Arnaud 1996). The interstellar absorption was modelled through the `TBabs` component, with the abundances provided by Wilms et al. (2000) and the cross sections of Verner et al. (1996). We derived the unabsorbed fluxes with the `cflux` convolution model.

#### 3.3.1. *NICER* and *Swift* monitoring

MAXI J1834–021 was monitored with an almost daily cadence by *NICER* during 2023. In this study, we report on the analysis of the first 81 pointings (see Table A.1). We analysed each spectrum individually, keeping the data in a range over which the source signal would lie above the background. This range varies between 0.5–8 keV and 0.5–5.5 keV, depending on the brightness of the source. All spectra were analysed using three models: one including only the Comptonisation spectrum (Model 0, `TBabs`×`nthComp`); and two others that include an additional thermal component, either a black body (Model 1A, `TBabs`×(`nthComp`+`bbodyrad`)), or a disc black body (Model 1B, `TBabs`×(`nthComp`+`diskbb`)). The black body scenario would be appropriate for an NS LMXB where the thermal emission arises from either the NS surface or the boundary layer surrounding it, while the disc black body scenario, where the thermal emission comes from the accretion disc, would apply to both BH and NS LMXBs. The outcome of an F-test on the statistical significance of adding the thermal component was used as a criterion to choose between Model 0 and Model 1A or 1B. In particular, whenever the probability of improvement by chance of the `bbodyrad` or `diskbb` component was estimated to be lower than $10^{-4}$, we considered the thermal emission significant and chose Model 1A or 1B instead of Model 0. When the thermal component was found to be statistically significant, we tied together the black body temperature $kT_{\rm bbody}$, or disc black body temperature $kT_{\rm disc}$, with the seed photon temperature $kT_{\rm seed}$, since the fits could not constrain both parameters independently. In all cases, we fixed the hydrogen column density $N_{\rm H}$ to $0.9 \times 10^{22}$ cm$^{-2}$ (i.e., the value obtained from the broadband spectral analysis with Model 3, see Sect. 3.3.3). The `inp_type` parameter was set to 0 for Model 1A, and 1 for Model 1B, to distinguish between black-body-like and disc-black-body-like distributions of seed photons, respectively. Additionally, since the lack of hard X-rays coverage prevented us from constraining the high-energy cutoff, the electron temperature $kT_{\rm e}$ was fixed to 100 keV in all models. In addition, MAXI J1834–021 was intensively monitored by *Swift*-XRT. To increase statistical quality, we merged observations carried out a few days apart (see TableA.1), resulting in 40 spectra. These spectra were fit simultaneously with Model 0. All parameters were allowed to vary between the datasets, except for $N_{\rm H}$, which was fixed at $0.9 \times 10^{22}$ cm$^{-2}$. The parameter $kT_{\rm seed}$ was also not constrained by the fit and was fixed at 0.1 keV. The *Swift* observations did not require an additional thermal component, most likely due to the low photon statistics of the single *Swift*-XRT observations.

The best-fitting values for the *NICER* and *Swift*-XRT spectra are listed in Tables B.1, B.2, and B.3. Figure 2 shows the temporal evolution of the spectral parameters and the unabsorbed flux derived in the 0.5–10 keV energy band. The general trends observed in the spectral parameters remain consistent regardless of whether a `diskbb` or a `bbodyrad` component is used to describe the thermal emission. The thermal components are statistically significant only during the brightest phases of the outburst. A correlation between the X-ray flux and the Γ index is evident in all fits, with the source exhibiting a softening trend as it becomes brighter in X-rays (see also Figure 3). The normalisations of the black body $K_{\rm bbody}$ and the disc black body $K_{\rm disc}$ components can be used to obtain an estimate of the size of these regions, as given by:

$$K_{\rm bbody} = \left(\frac{R_{\rm bb}}{D_{10\,\rm kpc}}\right)^2, \quad K_{\rm disc} = \left(\frac{R_{\rm in}}{D_{10\,\rm kpc}}\right)^2 \cos\theta, \tag{1}$$

where $R_{\rm bb}$ and $R_{\rm in}$ are expressed in km, $D_{10\,\rm kpc}$ is the distance in units of 10 kpc, and $\theta$ is the inclination angle of the system.

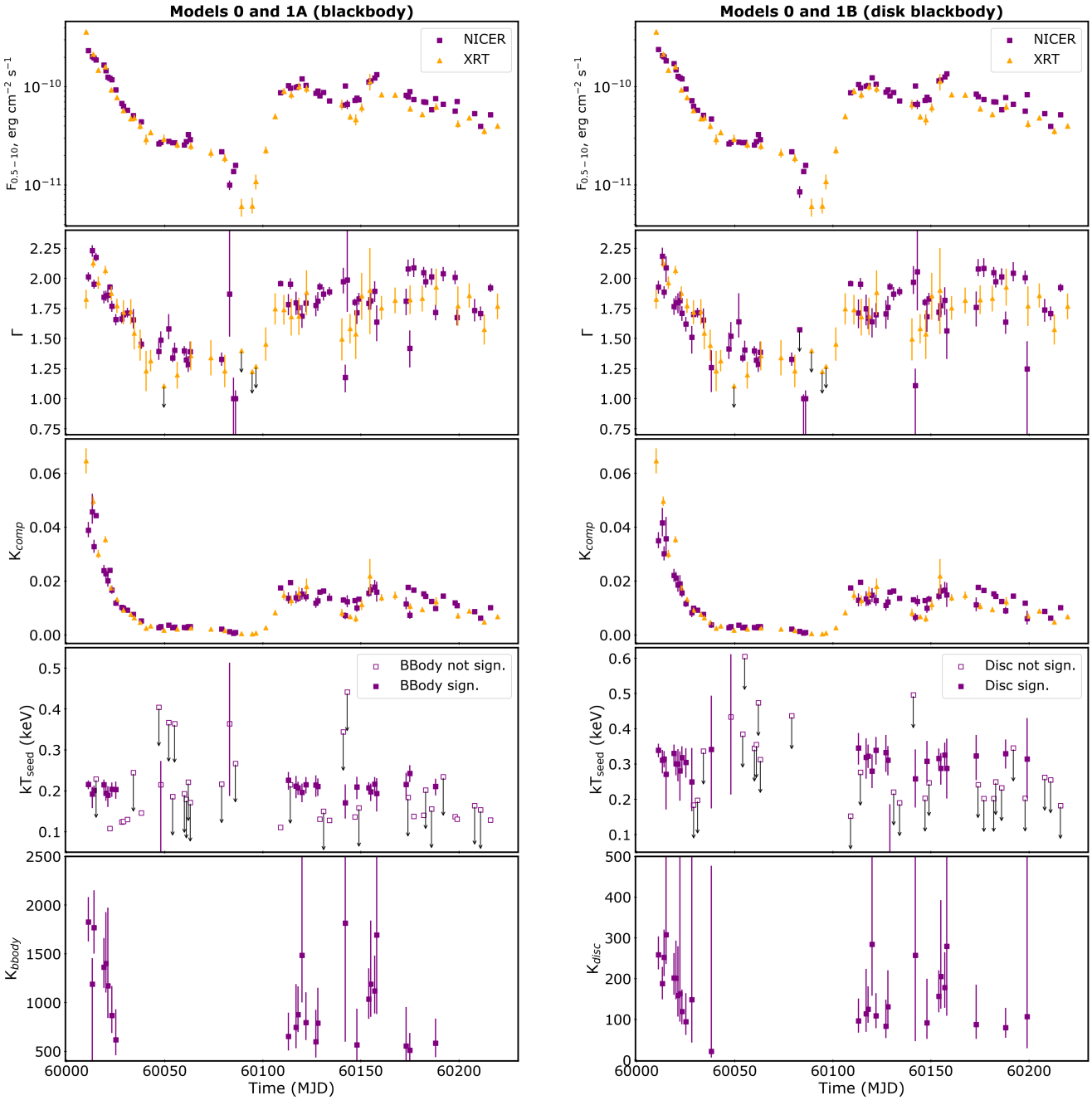


**Fig. 2.** Evolution of the main spectral parameters from the 2023 *NICER* and *Swift* campaign on MAXI J1834–021 with Models 0 and 1A (left) and 1B (right). The top panels show the unabsorbed flux in the 0.5–10 keV range as estimated from spectral fitting for both *NICER* (purple squares) and *Swift*-XRT (orange triangles). The evolution of the main best-fit parameters used in the spectral analysis (Sect. 3.3.1) is plotted in the other panels. In the fourth panel, filled and empty squares differentiate observations where the inclusion of the `bbodyrad`/`diskbb` component is significant (in chich case $kT_{\rm seed} = kT_{\rm bbody}$ or $kT_{\rm seed} = kT_{\rm disc}$) from those where it is not significant.

As the distance to the source is currently unknown, we calculated the radii for four possible distance values, as shown in Fig. 4. The inclination angle is also unknown, and is therefore fixed at 60 deg. The resulting size of the black body emitting region, which is several tens of kilometres for any tested distance value, would be more compatible with a boundary layer or a narrow disc-like region than, for example, a fraction of the NS surface. However, we caution that the lack of information on the distance and/or inclination of the source does not allow us to completely rule out the NS surface scenario. Given the practical equivalence between Models 1A and 1B and the indication of a disc-like emitting region, in the following sections, we mainly adopt Model 1B (`diskbb` as the thermal component).

### 3.3.2. Low-energy absorption feature

The first eight *NICER* spectra suggest the presence of an absorption feature at ~0.96 keV, as visible in the *NICER* and *NuSTAR* broadband spectrum in Figure 5a. To test its origin and significance, we merged the *NICER* observations with a compatible spectral index and similar hardness ratio. We repeated the procedure for three groups of observations:

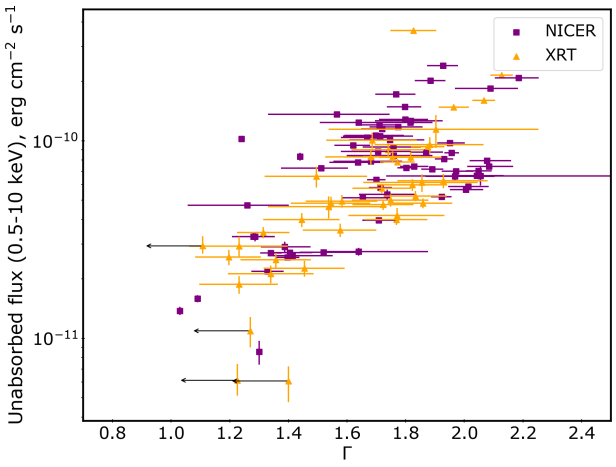


**Fig. 3.** Evolution of the best-fit power-law photon index Γ versus unabsorbed 0.5–10 keV flux for all *NICER* (purple squares) and *Swift*-XRT (orange triangles) observations. Data correspond to the results of the fits using Models 0–1B.

6203690101 to 6203690107, showing the highest hardness ratio; 6203690135 to 6203690141, showing the lowest hardness ratio; and 6203690157 to 6203690169, during the reflaring phase. We used Model 1B for the first and third groups, and Model 0 for the second group, as described in Section 3.3.1, with the addition of the `Gaussian` component (with negative normalisation) to model the feature. Therefore, the models read as `TBabs(nthComp + diskbb + gaussian)` and `TBabs(nthComp + gaussian)`, respectively. We estimated the significance of the feature as the ratio of its normalisation to the error at $1\sigma$ of the same parameter. The second group does not show any significant feature, while in the first and third groups we find a feature with significance of $\sim 4.2\sigma$ in the softest spectra and $\sim 2.6\sigma$ during the reflaring phase. In the first group, the feature is centred at $0.94^{+0.02}_{-0.07}$ keV, with width $\sigma_{\rm line} = 0.07^{+0.03}_{-0.03}$ keV and equivalent width $\sigma_{\rm eq} = 22.6^{+0.8}_{-0.9}$ eV. During the reflaring phase, we find $E_{\rm line} = 0.93^{+0.04}_{-0.05}$ keV, $\sigma_{\rm line} < 0.12$ keV, and $\sigma_{\rm eq} < 25.8$ eV.

To further investigate this spectral line, we inspected the *Swift*-XRT spectra. Individual spectra do not show evidence of the feature; therefore, we combined all spectra corresponding to the WT-mode observations. We fit the combined spectrum with Model 0 ($\chi^2_\nu = 1.3$ for 56 degrees of freedom) and structured residuals around 1 keV were visible. The inclusion of the `Gaussian` component improved the fit, resulting in $\chi^2_\nu = 1.1$ for 53 degrees of freedom (d.o.f.). The line parameters are: $E_{\rm line} = 0.96^{+0.04}_{-0.29}$ keV, $\sigma_{\rm line} < 0.41$ keV and $\sigma_{\rm eq} = 28 \pm 17$ eV, with a significance of $\sim 2\sigma$. We also merged the PC mode observations with consistent flux levels and did not find any hint of the absorption feature.

Given the evidence for the presence of the feature in both the *NICER* and *Swift* spectra, we retained this component in the modelling of the broadband spectrum (see Section 3.3.3). To employ a more sophisticated model for the absorption feature, we verified that modelling with the `Gaussian` component is equivalent to the modelling with the `gabs` component and ultimately adopted the latter option for our final version.

### 3.3.3. The *NICER* +*NuSTAR* broadband spectrum

We fit the *NICER* (OBSID: 6203690104) and *NuSTAR* spectra extracted from the simultaneous observations performed on March 10, 2023. We analysed the *NICER* observation in the 0.5–5.9 keV energy range (exposure time = 7.6 ks) and the *NuSTAR* data in the 3.0–60.0 keV energy range (Focal Plane Module A exposure time = 29.0 ks and Focal Plane Module B exposure time = 28.8 ks). Both energy ranges were chosen to limit our analysis to the intervals of the spectra that are dominated by the source emission. In all of the following models, we kept all parameters, including the photon index, linked between the spectra, and adopted a `constant` component (fixed at 1 for the *NICER* spectrum) to account for the differences between instruments.

Firstly, we tested Model 1B, with the addition of the `gabs` component as reported in Section 3.3.2, whose centroid was kept fixed at an energy of 0.97 keV. The electron temperature $kT_{\rm e}$ could not be constrained even in the broadband spectrum; therefore, we fixed it at 100 keV, which beyond the range covered by *NuSTAR*. We linked the disc temperature with the seed temperature of the Comptonised component and assumed that seed photons originate from within the accretion disc (i.e., we set the `inp_type` parameter to 1). As seen in Figure 5a, we note a more pronounced and rather large absorption feature at ~10 keV, likely an Fe K-edge, which we fit with an additional smeared edge (`smedge`) component. We limited the cut energy to values higher than 7 keV and fixed the smearing width to 2 keV. The new Model 1B for the broadband spectrum was therefore `TBabs × gabs × smedge(nthComp + diskbb)`. We also tried an alternative model replacing the `nthComp` model with a simpler convolution model (`simpl`). We note that the new version gives higher values for the normalisation of the Comptonised component. We named this version Model 2: `TBabs × gabs × smedge × simpl × diskbb`. After fitting Model 2 to the data, we still observe a slight excess in the residuals beyond 10 keV, potentially due to the Compton hump. This, along with the Fe K-edge, indicates the presence of reflection processes, even if there is no clear evidence of an iron line. We therefore added a reflection component, `relxillCp` (García et al. 2014), which substitutes the previous Comptonisation and smeared edge components (i.e., Model 3: `TBabs × gabs(diskbb + relxillCp)`). We kept the outer radius fixed at the default value of $400\,R_{\rm g}$ (where $R_{\rm g} = GM/c^2$ is the gravitational radius), linked to the break radius (defined as the radius at which the disc emissivity may change), and allowed the inner radius to vary. We also linked the emissivity indices and kept them at the default value of three (standard Shakura-Sunyaev disc, Shakura & Sunyaev 1973). The electron temperature $kT_{\rm e}$ was frozen at 100 keV since we could not constrain it within our energy range. We also fixed the density of the disc and the iron abundance ($n_{\rm e} = 10^{19}$ cm$^{-3}$, $A_{\rm Fe} = 1$ solar abundances from the default value). The ionisation parameter was left free to vary. The redshift was set to 0 (Galactic source). The adimensional spin was set to 0.99 (corresponding to the hypothesis of a maximally rotating BH), though Model 3 appears to be insensitive to its value. Since the fit could not constrain the inclination, we kept it fixed at 60 deg.

Table 1 lists the best-fit values for the broadband spectrum across all models investigated. The spectrum is already well modelled using a new version of Model 1B (Fig. 5b), which includes a Comptonised component with a spectral index $\Gamma \sim 1.8$, a disc temperature at the inner radius of ~0.4 keV, and a smeared Fe K-edge with a cut energy of ~7.5 keV ($\chi^2_\nu = 1.07$

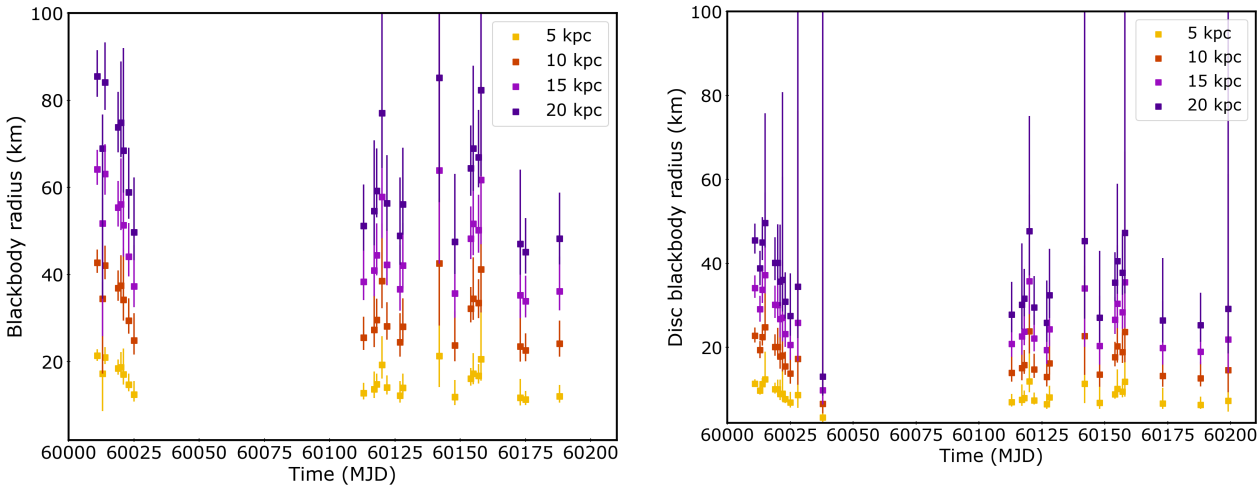


**Fig. 4.** Estimates of the sizes of the black body emitting region (Model 1A, left panel) and the disc (Model 1B, right panel), calculated from $K_{\rm bbody}$ and $K_{\rm disc}$, respectively.

for 405 d.o.f.). In the case of Model 2, the spectral index of the Comptonised component and the disc temperature are consistent with those of Model 1B. The fraction of up-scattered photons is ∼0.45. The absorption edge has a threshold energy of $\lesssim$7.8 keV. In the 0.5–60 keV energy band, the unabsorbed flux is $\sim 4 \times 10^{-10}$ erg cm$^{-2}$ s$^{-1}$. We obtain $\chi^2_\nu = 1.05$ for 405 d.o.f., which does not show a significant statistical improvement over Model 1B. However, the normalisation of the disc component increases substantially from ∼163 for Model 1B, to ∼345 for Model 2. Model 3 yields similar values for the spectral index and the disc temperature. We constrain the logarithm of the ionisation parameter of the disc matter to ∼3.7. We can determine only a $3\sigma$ upper limit on the disc inner radius of 11.4 $R_{\rm g}$. The unabsorbed flux in the 0.5–60 keV energy band remains $\sim 4 \times 10^{-10}$ erg cm$^{-2}$ s$^{-1}$.

### 3.4. Timing analysis

For the timing analysis, the photon arrival times of the source event files were referred to the Solar System barycentre using the `barycorr` tool, the latest calibration files, the ephemeris DE 405, and the coordinates derived in Section 3.1.

To probe the source short-term X-ray variability, we computed the PDS by normalising the power to the squared fractional root mean square (RMS) from *NuSTAR* and *NICER* event files using the 3–79 keV and 0.3–12 keV energy ranges, respectively, integrated over all frequencies. We applied the dead-time correction on the *NuSTAR* PDS using the Fourier Amplitude Difference (FAD) method (Bachetti & Huppenkothen 2018) as implemented in `Stingray` (Huppenkothen et al. 2019; Bachetti et al. 2024) and then extracted PDS by averaging over 50-s long segments with time bin of 0.5 ms. For *NICER* we used only observations with more than 5000 photons and split them into segments with a duration of 10 s and a timing resolution of 0.6 ms. The PDS created for each segment were averaged to produce an average PDS per observation. For each PDS, we estimated the fractional RMS over the entire frequency band by modelling the PDS in XSPEC with a combination of Lorentzian functions and a constant to account for the Poisson noise contribution. The RMS of the 3–79 keV *NuSTAR* PDS was 35 ± 4%, and we show the temporal evolution of the RMS for the 0.3–12 keV *NICER* PDS in Figure 6 (top panel). During the first 40 days of the monitoring campaign, the RMS did not show any particular trend, oscillating around an average of ∼25%. It reached its minimum (∼10%) when the flux was also at its lowest value. Subsequently, the RMS increased again and reached a constant value of ∼20% during the rebrightening phase. We detected a QPO in some of the *NICER* observations; two examples of PDS exhibiting this timing feature are displayed in Fig. 6 (middle panel). Using a Lorentzian component to model the QPO, we studied the temporal evolution of its best-fit centroid frequency $\nu_{\rm QPO}$, which decreased from ∼1.9 to 0.9 Hz in the first ∼20 days of our campaign, as shown in Fig. 6. In addition, an anti-correlation was found between $\nu_{\rm QPO}$ and the hardness ratio: when the former decayed, the latter increased until the rebrightening, when both quantities were constant. For the simultaneous *NICER* and *NuSTAR* observations, we extracted the PDS in the common energy band, 3–10 keV (see Fig. 6, bottom panel). The best fit $\nu_{\rm QPO}$ was 1.8 ± 0.2 Hz for *NICER* data and 1.9 ± 0.1 Hz for *NuSTAR* data, while the full width at half maximum was equal to $1.1^{+0.9}_{-0.5}$ Hz and 0.9 ± 0.3 Hz for the *NICER* and *NuSTAR* PDS, respectively.

We also searched for periodic signals in the *NuSTAR* observation, as well as in the first four *NICER* observations individually (i.e., those providing the largest counting statistics), using Fourier-domain acceleration search techniques. For each data set, we considered the entire energy range as well as distinct energy bands. We used the `accelsearch` pipeline from the `PRESTO`[4] pulsar timing software package (Ransom et al. 2002) to search for signals over the frequency range of 1–2000 Hz, summing up to 2, 4, and 8 harmonics. To account for potential power drifts in the Fourier domain, we allowed the powers of signals to drift by up to 200 frequency bins. Additionally, we tested the case where the powers of signals could drift by up to 600 frequency derivative bins (known as 'jerk' search; Andersen & Ransom 2018). This analysis was conducted on the entire observation dataset as well as on data chunks of 300 s. The identified candidate periodicities were sifted to reject less significant, duplicate, and/or harmonically related candidates. No statistically significant signal was detected.

[4] https://github.com/scottransom/presto

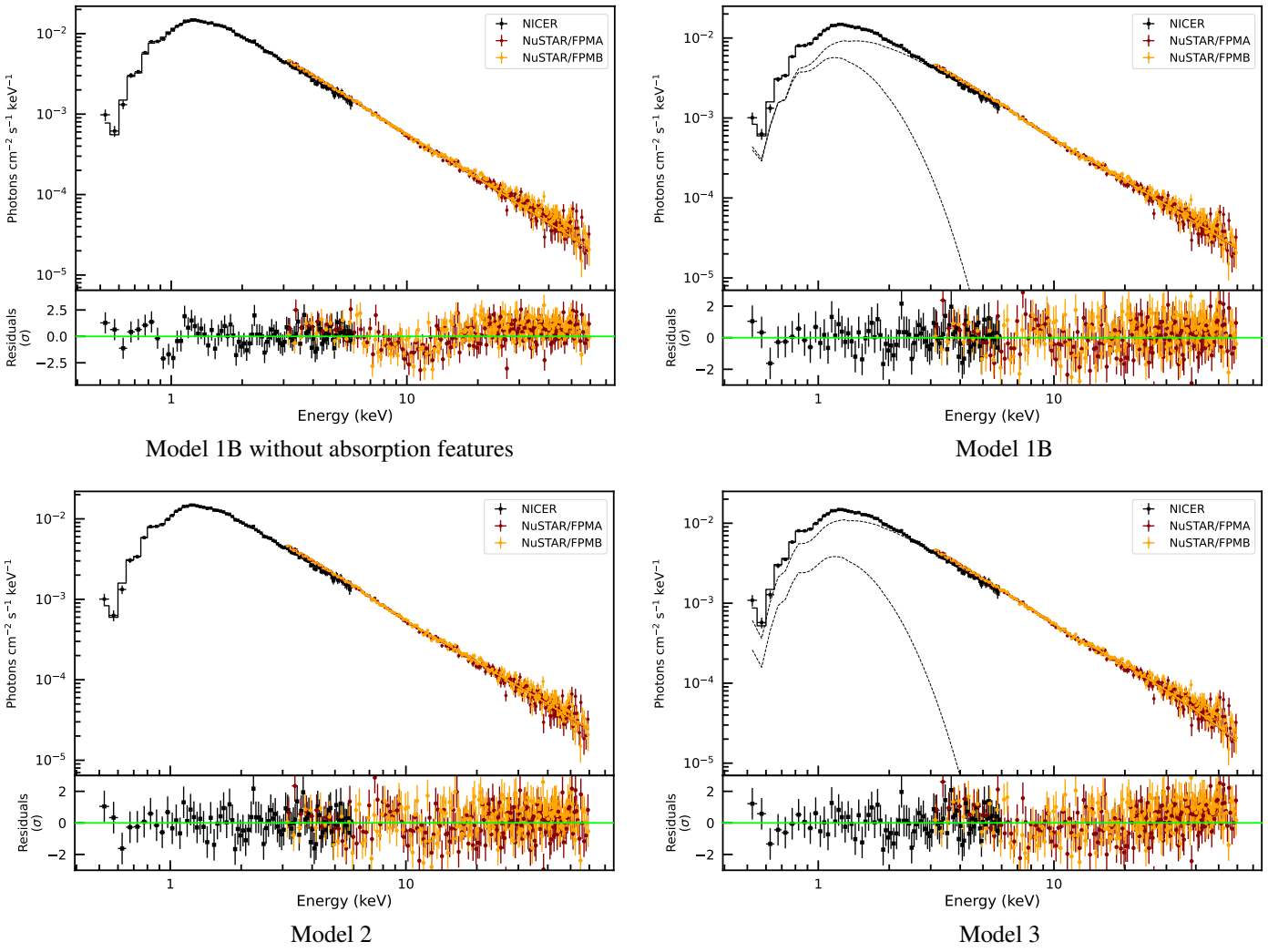


**Fig. 5.** Unfolded broadband spectrum (upper panel) and fit residuals (lower panel) extracted from *NICER* (black) + *NuSTAR*/FPMA (red) + *NuSTAR*/FPMB (orange) data over the 0.5–60 keV energy range. Panel (a) shows the fit without the inclusion of the absorption features (`TBabs(nthComp + diskbb)`). Panels (b) and (c) show the fit with Model 1B (`TBabs × gabs × smedge(nthComp + diskbb)`) and Model 2 (`TBabs × gabs × smedge × simpl × diskbb`), respectively. Panel (d) shows the fit with Model 3 (`TBabs × gabs(diskbb + relxillCp)`).

## 4. Discussion

We analysed the 2023 outburst of the X-ray transient MAXI J1834–021 with *NICER*, *NuSTAR*, and *Swift* data from March to October 2023. We conducted a spectral analysis of all single observations and a broadband *NICER* +*NuSTAR* spectrum. No NS observational signatures, such as type-I X-ray bursts or pulsations, were detected, ruling out the possibility of the presence of a BH. We also performed a timing analysis of the *NICER* and *NuSTAR* observations, deriving the value of the RMS to help determine the state of the system, and studying possible QPO components.

### 4.1. Outburst history: Evolution of the spectral parameters

Following its discovery in February 2023, MAXI J1834–021 was monitored for about 7 months, from March 3 to October 2, 2023, until it became no longer visible by both *Swift* and *NICER*. The source displayed a structured light curve with one main outburst observed mainly during its decay phase. The unabsorbed flux in the 0.5–10 keV energy range decreased from $\sim 2.5 \times 10^{-10}$ erg cm$^{-2}$ s$^{-1}$ to $5.5 \times 10^{-12}$ erg cm$^{-2}$ s$^{-1}$ over three months, followed by a fast rebrightening and a series of flux variations between $\sim 3.5{\times}10^{-11}$ and $7{\times}10^{-11}$ erg cm$^{-2}$ s$^{-1}$ (see Fig. 2, top panel). During the main outburst, both *NICER* and *Swift*-XRT spectra were dominated by a non-thermal component, well-described by a Comptonisation spectrum with $\Gamma \sim 1.5$–$2.2$. An additional thermal component, either a black body or a disc black body, was required in *NICER* data for the first 30 days of the monitored period, with a slight decrease in temperature from $\sim$0.4 keV to $\sim$0.3 keV. This thermal component later became not significant. The non-thermal nature of the spectrum suggests that during our monitoring campaign MAXI J1834–021 was in a hard or intermediate state; this classification is corroborated by the RMS values found during the campaign (e.g., Muñoz-Darias et al. 2011, 2014). It is noteworthy that follow-up X-ray observations were triggered only about a month after the initial *MAXI* detection, due to a delay in the announcement (Negoro et al. 2023). We checked whether a possible transition to a soft state could be detected in the *MAXI* data during the one-month delay. However, we did not find any clear softening in the light curve or hardness ratio. MAXI J1834–021 could be one of the transient X-ray binaries that underwent a failed-transition outburst (e.g. Alabarta et al. 2021). Around MJD 60100, the

**Table 1.** Best-fit values of the *NICER* + *NuSTAR* broadband spectrum.

| Component | Parameter | Model 1B | Model 2 | Model 3 |
|---|---|---|---|---|
| TBabs | $N_{\rm H}$ ($\times 10^{22}$ cm$^{-2}$) | $0.84^{+0.03}_{-0.03}$ | $0.84^{+0.02}_{-0.02}$ | $0.90^{+0.04}_{-0.01}$ |
| gabs | E (keV) | 0.97* | 0.97* | 0.97* |
| | $\sigma$ (keV) | $0.06^{+0.03}_{-0.04}$ | $0.05^{+0.04}_{-0.04}$ | $0.07^{+0.04}_{-0.04}$ |
| | Strength (keV) | $0.015^{+0.009}_{-0.007}$ | $0.015^{+0.008}_{-0.007}$ | $0.021^{+0.011}_{-0.009}$ |
| diskbb | $kT_{\rm disc}$ (keV) | $0.38^{+0.03}_{-0.03}$ | $0.37^{+0.02}_{-0.02}$ | $0.34^{+0.03}_{-0.04}$ |
| | $K_{\rm disc}$ | $163^{+66}_{-37}$ | $345^{+122}_{-80}$ | $177^{+226}_{-59}$ |
| nthComp | $\Gamma$ | $1.79^{+0.01}_{-0.01}$ | – | – |
| simpl | Scattered frac. | – | $0.45^{+0.02}_{-0.06}$ | – |
| | $\Gamma$ | – | $1.79^{+0.01}_{-0.02}$ | – |
| smedge | $E_{\rm edge}$ (keV) | $7.5^{+0.5}_{-0.5}$ | $\lesssim$7.8 | – |
| | Absorption depth | $0.26^{+0.04}_{-0.04}$ | $0.25^{+0.04}_{-0.04}$ | – |
| | Index for photo-electric cross-section | –2.67* | –2.67* | – |
| | Smearing width (keV) | 2* | 2* | – |
| relxillcp | $\Gamma$ | – | – | $1.72^{+0.01}_{-0.01}$ |
| | $R_{\rm in}$ ($R_g$) | – | – | <11.4 |
| | $A_{\rm Fe}$ ($A_\odot$) | – | – | 1* |
| | log $X_i$ | – | – | $3.69^{+0.03}_{-0.02}$ |
| | log ($n_{\rm e}$/cm$^{-3}$) | – | – | 19* |
| | Refl. frac. | – | – | >3 |
| Observed Flux ($\times 10^{-10}$ erg cm$^{-2}$ s$^{-1}$) | | $3.29^{+0.13}_{-0.03}$ | $3.31^{+0.14}_{-0.34}$ | $3.21^{+0.05}_{-0.28}$ |
| Unabsorbed Flux ($\times 10^{-10}$ erg cm$^{-2}$ s$^{-1}$) | | $3.78^{+0.28}_{-0.21}$ | $4.10^{+0.13}_{-0.11}$ | $4.06^{+0.05}_{-0.04}$ |
| $\chi^2$ (d.o.f.) | | 435.02(405) | 426.71(405) | 442.69(404) |

**Notes.** Fluxes are calculated in the 0.5–60 keV energy band. Models used are: Model 1B: TBabs × gabs × smedge(nthComp + diskbb), Model 2:TBabs × gabs × smedge × simpl × diskbb, Model 3: TBabs × gabs(diskbb + relxillCp). * Fixed parameter in the fit.

source rebrightened, undergoing a second, longer outburst that lasted until the end of the 2023 visibility window in October. These rebrightening or 'echo outbursts' (e.g. Zhang et al. 2019) have often been observed in both BHs (e.g., Cúneo et al. 2020) and NSs (e.g., Patruno et al. 2016). The rebrightening in MAXI J1834–021 never reached the flux level of the first main outburst, achieving a flux of $\sim 1 \times 10^{-10}$ erg cm$^{-2}$ s$^{-1}$ at peak, corresponding to 60% of the peak flux of the first activity phase. Interestingly, the pattern followed by the source in this second activity phase is rather erratic, with the flux swinging around an average level of $(5–6) \times 10^{-11}$ erg cm$^{-2}$ s$^{-1}$. We attempted to model all observations using both Model 0 and Models 1A and 1B, and found that only a subset of the spectra required the inclusion of a thermal component in the model, namely those collected during periods of flux increase. This behaviour is reminiscent of that observed in the BH MAXI J1348–630 during its 2019 reflare (Dai et al. 2023). In particular, these authors suggested that the disc began an ingress trend once the system exceeded a 'critical' luminosity of $\sim 2.5 \times 10^{36}$ erg s$^{-1}$. Assuming a similar critical threshold for our system, we can obtain a possible value for the distance for the source of about 19 kpc. We note that such a high distance could explain the radio non-detection of the source (see Section 4.3); however, given the many assumptions made to obtain this distance value, we caution that this should be taken more as a hint rather than an actual measurement.

### 4.2. Broadband spectrum and spectral features

The continuum of the broadband spectrum is described by a model composed of a multicolour disc black body and a Comptonised emission component. We could not constrain the electronic temperature within our energy range, suggesting that the high-energy cutoff might extend beyond 60 keV of the *NuSTAR* energy range. Such values for the high-energy cutoff are typical of BH systems, while for NS systems, the cutoff temperature is found within ~15–25 keV (Burke et al. 2017). The spectrum shows a dip at around ~10 keV, which we interpret as a potential smeared Fe K-edge. With the addition of a smeared edge component, we obtain a cut energy of ~7.5 keV, compatible with Fe K-shell recombination processes. Nonetheless, we find no evidence for the presence of an iron emission line. However, due to the evidence of a potential Fe K-edge, we included a reflection component in the model. The new model remains statistically equivalent to the previous model (see Table 1). The reflection component is not very strong and we could only obtain a lower limit on the ionisation parameter of log$X_i \gtrsim 3.7$, corresponding to highly ionised matter, and thus aligning with the absence of a detectable iron line at ~6.4 keV (for a description of the model, see García et al. 2014). We derive an upper limit for the inner radius of the accretion disc at ~11.4 $R_{\rm g}$, but the adimensional spin parameter cannot be properly determined. This does not exclude that the disc might extend to lower radii, as

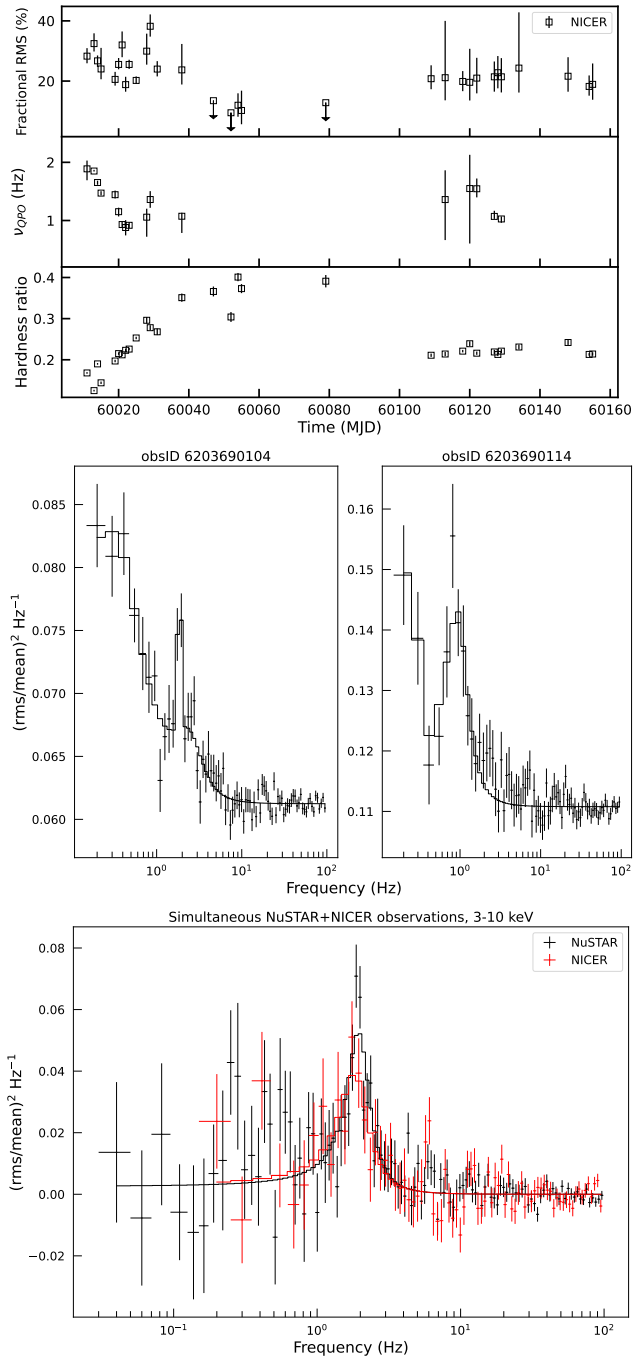


**Fig. 6.** Top: Temporal evolution of the RMS integrated over all frequencies (top panel) and QPO central frequency (medium panel), estimated from the 0.3–12 keV *NICER* PDS. The bottom panel presents the temporal evolution of the hardness ratio, as defined in Sect. 3.2. Middle: Two 0.3–12 keV *NICER* PDS showing the QPO for the highest (left, OBSID 6203690104) and lowest (right, OBSID 6203690114) central frequency $\nu_{\rm QPO}$. Poisson noise was not subtracted. Bottom: The PDS of the *NuSTAR* (black) and *NICER* (red) simultaneous observations in the common energy range of 3–10 keV. Poisson noise was subtracted for plotting purpose. The solid lines represent the best-fit models.

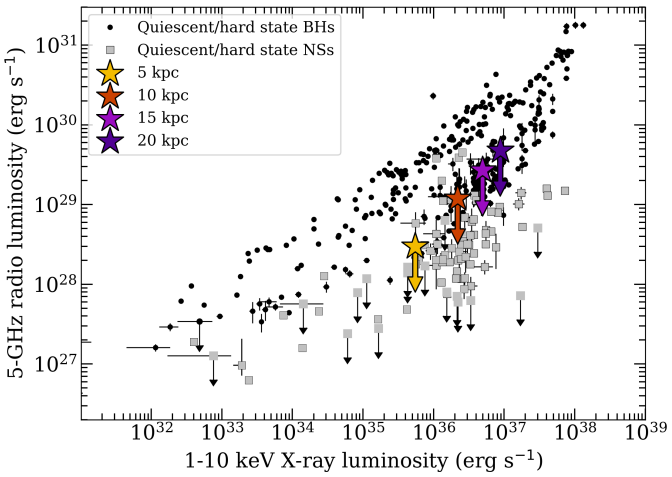


**Fig. 7.** Radio–X-ray luminosity diagram of quiescent and hard state BH transients (black circles) and NS (grey squares) LMXBs, plotted using the data repository from Bahramian et al. (2018). In the plot, the X-ray luminosity of MAXI J1834–021 and the upper limit on the radio luminosity obtained by Bright et al. (2023) are plotted as stars, colour-coded for different distances.

the radius derived from the reflection component corresponds to the radius at which recombination processes occur sufficiently to be detected, and does not necessarily match the inner radius of the disc (Krolik & Hawley 2002). A more meaningful comparison could be possible with the disc inner radius estimated from the thermal disc component of the model, but our derivation is currently affected by the lack of information on the inclination angle and source distance. We can only illustrate the dependence of the apparent inner radius on the unknown parameters. From the reflection component, we obtain an upper limit of $11.4R_g \simeq 17(M/M_\odot)$ km, corresponding to ∼24 km for a mass of $1.4\,M_\odot$ of the prototypical NS and ∼170 km for a BH of mass $10\,M_\odot$. Referring to the values reported in Table 1, while for Model 1B the normalisation is consistent with that of Model 3 (see Fig. 4), for Model 2 we obtain a normalisation of ∼345, corresponding to an inner radius of ∼13–39 km for an inclination angle of 60 deg and a distance D in the range 5–15 kpc.

We detected an absorption feature at ∼0.96 keV, both in the *NICER* spectra and in the merged *Swift*-XRT WT spectra. The feature has a significance of $\sim 4\sigma$ in the softest *NICER* spectra, and of $\sim 2\sigma$ in the *Swift* and *NICER* spectra collected during the reflaring phase. While we cannot entirely rule out the possibility of an instrumental origin for this feature, its detection in both *NICER* and *Swift* data, although with low significance, suggests it is not an artifact. A similar absorption feature at ∼1 keV was recently detected in *NICER* (Del Santo et al. 2023) and *XMM-Newton* (Del Santo et al., in prep.) observations of the BH candidate MAXI J1810–222. The authors explained the spectral feature as possible evidence of ultra-fast outflows from the system.

### 4.3. Nature of the source

The nature of the accretor in MAXI J1834–021 remains unclear. Type-I X-ray bursts or pulsations, incontrovertible signatures of the NS nature of the primary star, have not been detected in *NuSTAR*, *Swift*-XRT, or *NICER* data (Section 3.4). However, the absence of these features does not rule out the presence of an NS, since the majority of NS LMXBs are not X-ray pulsators, and type-I X-ray bursts can easily be missed (Di Salvo et al. 2022). In this context, X-ray spectral and timing properties can provide some clues, though they are not conclusive. During the hard-intermediate state, MAXI J1834–021 shows a relatively hard spectrum with $\Gamma \lesssim 1.7$ and high RMS values (never below 10%), which are typically found in BH systems in hard-intermediate states (see, e.g.,

Muñoz-Darias et al. 2011), although they are sometimes also displayed by NS systems (see, e.g., Muñoz-Darias et al. 2014).

A QPO is present at the beginning of the decay of the first activity phase with a central frequency decreasing from ∼1.9 to 0.9 Hz. The QPO also appears in a few observations during the rebrightening. Common in both BH and NS LMXBs, QPOs have been observed across a wide range of frequencies and have been classified into different types. The feature in the PDS of MAXI J1834–021 is characterised by a narrow peak, as observed for Type-C and Type-B QPOs in BH binaries (e.g., Motta et al. 2015). Type-C QPOs are accompanied by a strong flat-top noise component, while, Type-B QPOs generally appear in the PDS coincident with weak red noise. For the former, the central frequency is tightly correlated with the spectral state, rising from low mHz values in the hard state to ∼10 Hz in the intermediate states. For the latter, it is usually in the 5–8 Hz range, but in a few instances type-B QPOs were also found at 1–3 Hz. The archetypal BH binary GX 339–4 shows type-B QPOs at low frequencies (i.e. below ∼3 Hz, see Motta et al. 2011) during intermediate states, more specifically during the low luminosity soft-to-hard transition, which might be the case for MAXI J1834–021. However, GX 339–4 showed softer energy spectra and lower RMS values in correspondence with these low-frequency type-B QPOs than what we observed for MAXI J1834–021. Type C QPOs are also found at ∼1–2 Hz in GX,339–4 when RMS reaches values as high as those estimated for this new transient (Motta et al. 2011). For NS systems, the QPO phenomenology is richer. If the power spectral feature of MAXI J1834–021 were a normal branch oscillation, the centroid frequency would not match the expected values (∼5–6 Hz). However, there are quasi-periodic variability phenomena in NS LMXBs that do not have an equivalent in BH LMXBs. For example, QPOs at ∼1 Hz and at variable frequencies between 0.58 and 2.44 Hz were found in two NS LMXBs, 4U 1323–62 and EXO 0748-676, respectively (Jonker et al. 1999; Homan et al. 1999). The PDS of these two sources (see Fig. 2 in Jonker et al. 1999 and Fig. 1 in Homan et al. 1999) resemble that of MAXI J1834–021 and the QPO central frequencies are consistent. However, 4U 1323–62 and EXO 0748-676 are dipping systems, and the origin of the QPO is thought to be related to their high inclination. The light curves of MAXI J1834–021 did not show any dips and the inclination is unknown. From the timing analysis we performed, it is difficult to draw any conclusion about the origin of the QPO and the nature of the compact object of this new X-ray transient. Even though at the beginning of the decay the RMS seems to be roughly constant while the hardness ratio clearly increases, when the source enters a fainter state associated with high hardness, the RMS drops. During the rebrightening, a similar behaviour is detected: the RMS increases to 20% while the hardness drops. This does not resemble the typical behaviour of both accreting BHs and NSs, which show a positive correlation between total RMS and hardness (Muñoz-Darias et al. 2011, 2014).

Another rough indicator on the nature of the source is its location on the radio-X-ray luminosity plane. Both BH and NS LMXBs in the hard state are known to launch powerful jets, which can be observed in the radio-IR band. By plotting BH transients and NS-LMXB radio luminosity versus their X-ray luminosity, a clear correlation can be observed (e.g., Fender & Kuulkers 2001). Additionally, BH and NS LMXBs populate two different regions (although with significant overlap), with BH systems being systematically radio louder at the same X-ray luminosity (van den Eijnden et al. 2021). MAXI J1834–021 was observed by AMI-LA (central frequency of 15.5 GHz) during the main outburst on March 8, 2023. No radio counterpart was detected and a radio flux density upper limit of ∼200 μJy was established (Bright et al. 2023). The source was detected at a 0.5–10 keV unabsorbed flux of $\sim 2.3 \times 10^{-10}$ erg cm$^{-2}$ s$^{-1}$ on the same day by *NICER* (ObsID 6203690102; Table A.1). Since the distance of the source is unknown, we tentatively consider four values – 5, 10, 15, and 20 kpc – and obtain four distinct results for the position of the source on the radio–X-ray luminosity plane (Fig. 7). Unfortunately, lacking any meaningful constraint on the source distance, the position of the source on the radio– X-ray luminosity diagram is rather ambiguous. If the source is located beyond 15 kpc, the upper limit is consistent with MAXI J1834–021 being a distant BH, as also suggested in Section 4.1 and by Homan et al. (2023), although a radio-bright NS cannot be ruled out. This situation is reminiscent of that found for MAXI J1810–222, which was suggested to be a relatively distant BH transient, also based on its radio–X-ray location (Russell et al. 2022). If the system is instead closer, within 10 kpc, the source could be an exceptionally radio-quiet BH X-ray binary or more likely an NS.

## 5. Conclusions

In this study, we analysed the 2023 outburst of the X-ray transient MAXI J1834–021 using data from *NICER*, *NuSTAR*, and *Swift*. Our investigation focused on the spectral properties and temporal variability of the source to determine its nature and behaviour during the outburst. Our key findings are summarised as follows.

- The source exhibited a complex outburst pattern with two major phases: an initial outburst followed by a rebrightening phase. During the outburst, the X-ray spectra were dominated by a Comptonisation component, roughly consistent with a power-law model with a photon index ranging from 1.5 to 2.2. The seed photons are probably provided by an accretion disc or a boundary layer, which is directly observed only during the brightest phases of the whole outburst, with temperature around 0.4 keV. When the disc is not visible, the temperature of the seed photons is also poorly constrained, possibly becoming too cold to be detected by *NICER*. An absorption feature around 0.96 keV was consistently observed in both *NICER* and *Swift* data, possibly indicating the presence of a wind, although its low significance prevents us from making a definitive interpretation on the nature of this feature.
- The broadband spectrum (0.5–60 keV) was well modelled by a combination of a multicolour disc black body and a Comptonised emission component, while we could not constrain the electronic temperature. The inclusion of a reflection component in the spectral model suggested a high ionisation parameter ($\log X_i \sim 3.7$) and provided an upper limit for the inner radius of the accretion disc at ∼11.4 gravitational radii. The reflection fraction was not well constrained, indicating that reflection processes, although present, were not dominant.
- A QPO with a centroid frequency varying between ∼1.9 and 0.9 Hz was detected and found to anti-correlate with the hardness ratio. The total RMS is constant while the hardness increases and the flux decreases, then drops when the hardness reaches its peak value.
- Although no radio counterpart was detected, the radio luminosity upper limit, combined with X-ray luminosity data, positioned the source in a region on the radio–X-ray luminosity plane that is consistent both with a distant BH transient and a radio-bright NS.

Overall, our detailed analysis of MAXI J1834–021 during its 2023 outburst did not provide substantial evidence for the classification of the compact object. While the spectral analysis appears to point towards a BH nature, the timing results and the radio upper limit do not allow us to rule out the NS scenario. Future, more sensitive observations during the next outburst from this source, particularly in the optical and radio wavelengths, as well as continued X-ray monitoring, will be crucial to further constrain the nature of this intriguing X-ray transient and to understand the mechanisms driving its complex outburst behaviour.

*Acknowledgements.* The authors acknowledge financial contribution from the agreement ASI-INAF n. 2017-14-H.0 and INAF mainstream (PI: A. De Rosa, T. Belloni), from the HERMES project financed by the Italian Space Agency (ASI) Agreement n. 2016/13 U.O and from the ASI-INAF Accordo Attuativo HERMES Technologic Pathfinder n. 2018-10-H.1-2020. We also acknowledge support from the European Union Horizon 2020 Research and Innovation Frame-work Programme under grant agreement HERMES-Scientific Pathfinder n. 821896 and from PRIN-INAF 2019 with the project "Probing the geometry of accretion: from theory to observations" (PI: Belloni). We thank the NuSTAR PI, Fiona Harrison, for approving the DDT request, and the NuSTAR SOC for carrying out the observation. We also thank Brad Cenko and the Swift duty scientists and science planners for making the Swift Target of Opportunity observations possible. A. Marino and F.C.Z. are supported by the H2020 ERC Consolidator Grant "MAGNESIA" under grant agreement No. 817661 (PI: Rea) and from grant SGR2021-01269 (PI: Graber/Rea). F.C.Z. is also supported by a Ramón y Cajal fellowship (grant agreement RYC2021-030888-I). A.B. is supported by the Spanish Ministry of Science under the grant EUR2021-122010 (PI: Muñoz-Darias), a L'Oreal–Unesco For Women In Science Fellowship (2023 Italian program) and ESA Fellowship. G.M. acknowledges financial support from the European Union's Horizon Europe research and innovation programme under the Marie Skłodowska-Curie grant agreement No. 101107057. M.A.P. acknowledges support through the Ramón y Cajal grant RYC2022-035388-I, funded by MCIU/AEI/10.13039/501100011033 and FSE+. T.M.-D. acknowledges support by the Spanish *Agencia estatal de investigación* via PID2021-124879NB-I00. This work was also partially supported by the program Unidad de Excelencia Maria de Maeztu CEX2020-001058-M. M.C.B. acknowledges support from the INAF-Astrofit fellowship.

## References

Alabarta, K., Altamirano, D., Méndez, M., et al. 2021, MNRAS, 507, 5507
Altamirano, D., van der Klis, M., Méndez, M., et al. 2008, ApJ, 685, 436
Andersen, B. C., & Ransom, S. M. 2018, ApJ, 863, L13
Arnaud, K. A. 1996, in Astronomical Data Analysis Software and Systems V, eds. G. H. Jacoby, & J. Barnes, Astronomical Society of the Pacific Conference Series, 101, 17
Bachetti, M., & Huppenkothen, D. 2018, ApJ, 853, L21
Bachetti, M., Huppenkothen, D., Stevens, A., et al. 2024, J. Open Source Softw., 9, 7389
Bahramian, A., & Degenaar, N. 2023, in Handbook of X-ray and Gamma-ray Astrophysics, eds. C. Bambi, & A. Santangelo, 120
Bahramian, A., Miller-Jones, J., Strader, J., et al. 2018, https://doi.org/10.5281/zenodo.1252036
Bassi, T., Del Santo, M., D'Aì, A., et al. 2019, MNRAS, 482, 1587
Belloni, T. M., & Motta, S. E. 2016, in Astrophysics of Black Holes (Springer Berlin Heidelberg), 61
Bhattacharyya, S., & Strohmayer, T. E. 2007, ApJ, 664, L103
Bright, J., Fender, R., Green, D., Alexander, P., & Titterington, D. 2023, ATel, 15939, 1
Burke, M. J., Gilfanov, M., & Sunyaev, R. 2017, MNRAS, 466, 194
Cackett, E. M., Miller, J. M., Bhattacharyya, S., et al. 2008, ApJ, 674, 415
Campana, S., Coti Zelati, F., & D'Avanzo, P. 2013, MNRAS, 432, 1695
Capitanio, F., Belloni, T., Del Santo, M., & Ubertini, P. 2009, MNRAS, 398, 1194
Casella, P., Belloni, T., & Stella, L. 2005, ApJ, 629, 403
Chelovekov, I., & Grebenev, S. 2010, arXiv e-prints [arXiv:1004.4086]
Cúneo, V. A., Alabarta, K., Zhang, L., et al. 2020, MNRAS, 496, 1001
Dai, X., Kong, L., Bu, Q., et al. 2023, MNRAS, 521, 2692
Degenaar, N., Medin, Z., Cumming, A., et al. 2014, ApJ, 791, 47
Degenaar, N., Ootes, L. S., Reynolds, M. T., Wijnands, R., & Page, D. 2017, MNRAS, 465, L10
Del Santo, M., Belloni, T. M., Tomsick, J. A., et al. 2016, MNRAS, 456, 3585
Del Santo, M., Pinto, C., Marino, A., et al. 2023, MNRAS, 523, L15
Di Salvo, T., & Sanna, A. 2022, in Accretion Powered X-ray Millisecond Pulsars, eds. S. Bhattacharyya, A. Papitto, & D. Bhattacharya, Astrophysics and Space Science Library, 465, 87
Di Salvo, T., Papitto, A., Marino, A., Iaria, R., & Burderi, L. 2022, in Low-Magnetic-Field Neutron Stars in X-ray Binaries, eds. C. Bambi, & A. Santangelo (Singapore: Springer Nature Singapore), 1
Esin, A. A., McClintock, J. E., & Narayan, R. 1997, ApJ, 489, 865
Evans, P. A., Beardmore, A. P., Page, K. L., et al. 2009, MNRAS, 397, 1177
Fabian, A. C., Rees, M. J., Stella, L., & White, N. E. 1989, MNRAS, 238, 729
Fender, R. P., & Kuulkers, E. 2001, MNRAS, 324, 923
Fortin, F., García, F., Simaz Bunzel, A., & Chaty, S. 2023, A&A, 671, A149
Galloway, D. K., & Keek, L. 2021, in Thermonuclear X-ray Bursts, eds. T. M. Belloni, M. Méndez, & C. Zhang, Astrophysics and Space Science Library, 461, 209
García, J., Dauser, T., Lohfink, A., et al. 2014, ApJ, 782, 76
García, J. A., Tomsick, J. A., Sridhar, N., et al. 2019, ApJ, 885, 48
Gavras, P., Rimoldini, L., Nienartowicz, K., et al. 2023, A&A, 674, A22
Gendreau, K. C., Arzoumanian, Z., Adkins, P. W., et al. 2016, in Space Telescopes and Instrumentation 2016: Ultraviolet to Gamma Ray, eds. J. W. A. den Herder, T. Takahashi, M. Bautz, Society of Photo-Optical Instrumentation Engineers (SPIE) Conference Series, 9905, 99051H
Harrison, F. A., Craig, W. W., Christensen, F. E., et al. 2013, ApJ, 770, 103
Homan, J., Jonker, P. G., Wijnands, R., van der Klis, M., & van Paradijs, J. 1999, ApJ, 516, L91
Homan, J., van der Klis, M., Fridriksson, J. K., et al. 2010, ApJ, 719, 201
Homan, J., Gendreau, K., Arzoumanian, Z., et al. 2023, ATel, 15951, 1
Huppenkothen, D., Bachetti, M., Stevens, A. L., et al. 2019, ApJ, 881, 39
Ingram, A., & Motta, S. 2014, MNRAS, 444, 2065
Ingram, A. R., & Motta, S. E. 2019, New Astron. Rev., 85, 101524
Ingram, A., Done, C., & Fragile, P. C. 2009, MNRAS, 397, L101
Jonker, P. G., van der Klis, M., & Wijnands, R. 1999, ApJ, 511, L41
Kaastra, J. S., & Bleeker, J. A. M. 2016, A&A, 587, A151
Karino, S., Nakamura, K., & Taani, A. 2019, PASJ, 71, 58
Krolik, J. H., & Hawley, J. F. 2002, ApJ, 573, 754
Lewin, W. H. G., & Clark, G. W. 1980, in Ninth Texas Symposium on Relativistic Astrophysics, 336, 451
Lewin, W., & van der Klis, M. 2006, Compact Stellar X-ray Sources (Cambridge, UK: Cambridge University Press)
Manca, A., Gambino, A. F., Sanna, A., et al. 2023a, MNRAS, 519, 2309
Manca, A., Sanna, A., Marino, A., et al. 2023b, MNRAS, 526, 1154
Marcel, G., Ferreira, J., Petrucci, P. O., et al. 2022, A&A, 659, A194
Marino, A., Anitra, A., Mazzola, S. M., et al. 2022, MNRAS, 515, 3838
Marino, A., Borghese, A., Coti Zelati, F., Rea, N., & Sanna, A. 2023, ATel, 15946, 1
Miyamoto, S., Kitamoto, S., Hayashida, K., & Egoshi, W. 1995, ApJ, 442, L13
Motta, S., Muñoz-Darias, T., Casella, P., Belloni, T., & Homan, J. 2011, MNRAS, 418, 2292
Motta, S. E., Casella, P., Henze, M., et al. 2015, MNRAS, 447, 2059
Motta, S. E., Rouco Escorial, A., Kuulkers, E., Muñoz-Darias, T., & Sanna, A. 2017, MNRAS, 468, 2311
Motta, S. E., Rodriguez, J., Jourdain, E., et al. 2021, New Astron. Rev., 93, 101618
Muñoz-Darias, T., Motta, S., & Belloni, T. M. 2011, MNRAS, 410, 679
Muñoz-Darias, T., Fender, R. P., Motta, S. E., & Belloni, T. M. 2014, MNRAS, 443, 3270
Negoro, H., Nakajima, M., Kobayashi, K., et al. 2023, ATel, 15929, 1
Patruno, A., Maitra, D., Curran, P. A., et al. 2016, ApJ, 817, 100
Ransom, S. M., Eikenberry, S. S., & Middleditch, J. 2002, AJ, 124, 1788
Remillard, R. A., Sobczak, G. J., Muno, M. P., & McClintock, J. E. 2002, ApJ, 564, 962
Russell, T. D., Del Santo, M., Marino, A., et al. 2022, MNRAS, 513, 6196
Saikia, P., Russell, D. M., Alabarta, K., Baglio, M. C., & Lewis, F. 2023, ATel, 15940, 1
Shakura, N. I., & Sunyaev, R. A. 1973, A&A, 24, 337
Tetarenko, B. E., Sivakoff, G. R., Heinke, C. O., & Gladstone, J. C. 2016, ApJS, 222, 15
van den Eijnden, J., Degenaar, N., Russell, T. D., et al. 2021, MNRAS, 507, 3899
van der Klis, M. 1989, in Two Topics in X-Ray Astronomy, Volume 1: X Ray Binaries. Volume 2: AGN and the X Ray Background, eds. J. Hunt, & B. Battrick, ESA Special Publication, 1, 203
van der Klis, M. 2006, in Compact stellar X-ray sources, eds. W. H. G. Lewin, & M. van der Klis, 39, 39
Verner, D. A., Ferland, G. J., Korista, K. T., & Yakovlev, D. G. 1996, ApJ, 465, 487
Wang, P. J., Kong, L. D., Chen, Y. P., et al. 2022, MNRAS, 512, 4541
Wijnands, R., Homan, J., & van der Klis, M. 1999, ApJ, 526, L33
Wilms, J., Allen, A., & McCray, R. 2000, ApJ, 542, 914
Zhang, G. B., Bernardini, F., Russell, D. M., et al. 2019, ApJ, 876, 5

## Appendix A: Log of X-ray observations

Table A.1 reports a journal of the X-ray observations of MAXI J1834–021 analysed in this work.

**Table A.1.** Log of the X-ray observations of MAXI J1834–021 analysed in this work.

| X-ray Instrument* | Obs.ID | Start YYYY-MM-DD hh:mm:ss (TT) | Stop YYYY-MM-DD hh:mm:ss (TT) | Exposure (ks) | Count Rate† (counts $s^{-1}$) |
|---|---|---|---|---|---|
| *Swift*-XRT (PC) | 00015914001 | 2023-03-06 19:05:35 | 2023-03-06 21:50:29 | 3.4 | 0.48±0.01 |
| *NICER*/XTI | 6203690102 | 2023-03-08 00:45:24 | 2023-03-08 22:48:40 | 6.1 | 26.54±0.08 |
| *NICER*/XTI | 6203690104 | 2023-03-10 05:25:48 | 2023-03-10 21:15:41 | 7.6 | 25.98±0.08 |
| *NuSTAR*/FPMA | 90901309002 | 2023-03-10 05:41:09 | 2023-03-10 21:16:09 | 29.0 | 2.68±0.01 |
| *NuSTAR*/FPMB | 90901309002 | 2023-03-10 05:41:09 | 2023-03-10 21:16:09 | 28.8 | 2.494±0.009 |
| *Swift*-XRT (WT) | 00089604001 | 2023-03-10 10:06:00 | 2023-03-10 12:08:56 | 3.2 | 2.31±0.03 |
| *NICER*/XTI | 6203690105 | 2023-03-11 03:07:49 | 2023-03-11 18:58:00 | 3.9 | 30.39±0.10 |
| *NICER*/XTI | 6203690106 | 2023-03-12 08:34:21 | 2023-03-12 09:17:00 | 1.3 | 26.40±0.36 |
| *Swift*-XRT (WT) | 00089604002 | 2023-03-13 00:06:15 | 2023-03-13 06:47:55 | 2.9 | 1.34±0.02 |
| *NICER*/XTI | 6203690110 | 2023-03-16 05:50:40 | 2023-03-16 20:11:40 | 2.5 | 24.75±0.11 |
| *Swift*-XRT (WT) | 00089604003 | 2023-03-16 13:50:09 | 2023-03-16 20:38:56 | 3.2 | 2.05±0.03 |
| *NICER*/XTI | 6203690111 | 2023-03-17 00:06:14 | 2023-03-17 19:11:22 | 3.0 | 22.06±0.09 |
| *NICER*/XTI | 6203690112 | 2023-03-18 15:17:00 | 2023-03-18 23:17:39 | 2.2 | 19.13±0.11 |
| *NICER*/XTI | 6203690113 | 2023-03-19 03:33:00 | 2023-03-19 20:57:40 | 1.7 | 18.14±0.11 |
| *Swift*-XRT (WT) | 00089604004 | 2023-03-19 11:43:15 | 2023-03-19 21:39:56 | 3.1 | 1.13±0.02 |
| *NICER*/XTI | 6203690114 | 2023-03-20 08:38:43 | 2023-03-20 18:38:40 | 3.3 | 17.29±0.08 |
| *Swift*-XRT (WT) | 00089604005 | 2023-03-22 06:33:04 | 2023-03-22 23:59:56 | 3.0 | 0.92±0.02 |
| *NICER*/XTI | 6203690116 | 2023-03-22 10:14:33 | 2023-03-22 21:37:26 | 3.3 | 13.23±0.07 |
| *NICER*/XTI | 6203690119 | 2023-03-25 18:49:50 | 2023-03-25 19:15:20 | 1.4 | 10.43±0.10 |
| *Swift*-XRT (WT) | 00089604006 | 2023-03-25T23:24:47 | 2023-03-25 23:50:56 | 1.7 | 0.73±0.02 |
| *NICER*/XTI | 6203690120 | 2023-03-26 07:13:34 | 2023-03-26 19:58:40 | 1.6 | 9.43±0.08 |
| *NICER*/XTI | 6203690122 | 2023-03-28 10:51:18 | 2023-03-28 15:21:30 | 1.0 | 8.60±0.10 |
| *Swift*-XRT (WT) | 00089604007 | 2023-03-29 16:09:28 | 2023-03-2916:36:56 | 1.6 | 0.60±0.02 |
| *Swift*-XRT (PC) | 00089604008 | 2023-03-31 03:11:06 | 2023-03-31 14:41:53 | 1.0 | 0.48±0.02 |
| *NICER*/XTI | 6203690123 | 2023-03-31 22:03:41 | 2023-03-31 22:43:20 | 0.5 | 7.77±0.14 |
| *Swift*-XRT (PC) | 00089604009 | 2023-04-03 06:08:38 | 2023-04-03 17:26:53 | 1.3 | 0.39±0.02 |
| *NICER*/XTI | 6203690124 | 2023-04-04 22:21:00 | 2023-04-04 22:50:40 | 1.4 | 5.63±0.07 |
| *Swift*-XRT (PC) | 00089604010 | 2023-04-06 02:09:44 | 2023-04-06 18:14:53 | 1.7 | 0.18±0.02 |
| *Swift*-XRT (PC) | 00089604011 | 2023-04-08 14:47:13 | 2023-04-08 20:59:53 | 2.9 | 0.32±0.01 |
| *NICER*/XTI | 6203690130 | 2023-04-13 12:28:40 | 2023-04-13 14:24:20 | 1.8 | 3.39±0.05 |
| *Swift*-XRT (PC) | 00089604012 | 2023-04-15 07:12:23 | 2023-04-15 20:02:53 | 1.7 | 0.23±0.01 |
| *NICER*/XTI | 6203690134 | 2023-04-18 15:59:39 | 2023-04-18 17:53:00 | 1.2 | 4.03±0.07 |
| *NICER*/XTI | 6203690135 | 2023-04-20 13:04:00 | 2023-04-20 22:45:20 | 3.1 | 3.37±0.04 |
| *NICER*/XTI | 6203690136 | 2023-04-21 07:32:40 | 2023-04-21 18:50:00 | 2.2 | 3.54±0.05 |
| *Swift*-XRT (PC) | 00089604013 | 2023-04-22 05:48:06 | 2023-04-22 13:59:53 | 2.7 | 0.23±0.01 |
| *NICER*/XTI | 6203690137 | 2023-04-26 05:21:20 | 2023-04-26 14:59:20 | 3.1 | 3.28±0.04 |
| *NICER*/XTI | 6203690139 | 2023-04-28 06:51:40 | 2023-04-28 23:51:45 | 0.8 | 4.19±0.08 |
| *Swift*-XRT (PC) | 00089604014 | 2023-04-28 15:29:00 | 2023-04-29 20:25:52 | 2.8 | 0.23±0.01 |
| *NICER*/XTI | 6203690140 | 2023-04-29 13:50:20 | 2023-04-29 17:04:40 | 0.7 | 3.96±0.09 |
| *Swift*-XRT (PC) | 00089604015 | 2023-05-09 02:31:53 | 2023-05-09 23:03:53 | 2.4 | 0.19±0.01 |
| *NICER*/XTI | 6203690145 | 2023-05-15 00:08:40 | 2023-05-15 14:30:40 | 1.9 | 2.68±0.05 |
| *Swift*-XRT (PC) | 00089604016 | 2023-05-16 06:09:22 | 2023-05-16 23:23:52 | 2.9 | 0.16±0.01 |
| *NICER*/XTI | 6203690149 | 2023-05-19 06:18:08 | 2023-05-19 17:17:00 | 0.7 | 1.66±0.06 |
| *NICER*/XTI | 6203690151 | 2023-05-21 01:39:15 | 2023-05-21 20:35:00 | 1.2 | 1.59±0.05 |
| *NICER*/XTI | 6203690152 | 2023-05-22 10:24:20 | 2023-05-22 23:00:20 | 1.2 | 1.71±0.05 |
| *Swift*-XRT (PC) | 00089604017‡ | 2023-05-24 02:57:29 | 2023-05-24 14:14:52 | 0.7 | 0.05±0.01 |
| *Swift*-XRT (PC) | 00089604018‡ | 2023-05-25 00:56:26 | 2023-05-26 01:05:52 | 2.2 | 0.053±0.004 |
| *Swift*-XRT (PC) | 00089604019 | 2023-05-30 06:08:10 | 2023-05-30 20:33:52 | 3.2 | 0.037±0.004 |
| *Swift*-XRT (PC) | 00089604020 | 2023-06-01 03:04:52 | 2023-06-01 20:38:52 | 1.7 | 0.097±0.008 |
| *Swift*-XRT (PC) | 00089604021 | 2023-06-06 02:00:02 | 2023-06-06 22:34:53 | 2.2 | 0.21±0.01 |
| *Swift*-XRT (PC) | 00016073002 | 2023-06-11 02:35:40 | 2023-06-11 12:11:52 | 1.7 | 0.43±0.02 |
| *NICER*/XTI | 6203690157 | 2023-06-14 09:13:00 | 2023-06-14 09:49:00 | 1.8 | 13.89±0.10 |
| *Swift*-XRT (PC) | 00016073003 | 2023-06-15 17:18:24 | 2023-06-15 17:42:53 | 1.5 | 0.43±0.02 |

**Table A.1.** Continued.

| X-ray Instrument* | Obs.ID | Start | Stop | Exposure | Count Rate† |
|---|---|---|---|---|---|
| | | YYYY-MM-DD hh:mm:ss (TT) | | (ks) | (counts $s^{-1}$) |
| *NICER*/XTI | 6203690159 | 2023-06-18 06:07:13 | 2023-06-18 06:36:51 | 1.1 | 16.65±0.13 |
| *Swift*-XRT (PC) | 00016073004 | 2023-06-19 00:52:31 | 2023-06-19 21:21:06 | 1.0 | 0.46±0.02 |
| *NICER*/XTI | 6203690160 | 2023-06-19 05:38:00 | 2023-06-19 06:02:00 | 0.5 | 15.47±0.17 |
| *NICER*/XTI | 6203690162 | 2023-06-22 01:48:40 | 2023-06-22 09:54:20 | 0.9 | 13.46±0.13 |
| *NICER*/XTI | 6203690163 | 2023-06-23 02:14:21 | 2023-06-23 13:31:39 | 2.8 | 15.69±0.09 |
| *Swift*-XRT (PC) | 00016073005 | 2023-06-23 03:29:06 | 2023-06-23 12:55:56 | 0.9 | 0.46±0.02 |
| *NICER*/XTI | 6203690165 | 2023-06-25 03:47:41 | 2023-06-25 16:30:40 | 0.7 | 18.48±0.18 |
| *Swift*-XRT (PC) | 00016073006 | 2023-06-27 02:20:55 | 2023-06-27 12:09:52 | 0.8 | 0.48±0.03 |
| *NICER*/XTI | 6203690166 | 2023-06-27 08:34:00 | 2023-06-27 14:55:20 | 1.6 | 16.71±0.11 |
| *NICER*/XTI | 6203690169 | 2023-07-02 04:42:30 | 2023-07-02 05:05:44 | 1.3 | 11.61±0.10 |
| *NICER*/XTI | 6203690170 | 2023-07-03 10:08:25 | 2023-07-03 10:29:40 | 1.3 | 14.63±0.12 |
| *NICER*/XTI | 6203690171 | 2023-07-04 04:57:01 | 2023-07-04 08:09:19 | 1.2 | 12.22±0.11 |
| *NICER*/XTI | 6203690172 | 2023-07-06 23:31:36 | 2023-07-06 23:37:02 | 0.3 | 14.00±0.22 |
| *NICER*/XTI | 6203690173 | 2023-07-09 08:45:07 | 2023-07-09 10:25:02 | 0.9 | 11.31±0.12 |
| *Swift*-XRT (PC) | 00016073007 | 2023-07-14 13:03:50 | 2023-07-15 22:57:53 | 0.4 | 0.68±0.04 |
| *NICER*/XTI | 6203690179 | 2023-07-16 11:18:31 | 2023-07-16 11:22:20 | 0.2 | 11.08±0.23 |
| *NICER*/XTI | 6203690180 | 2023-07-17 10:31:00 | 2023-07-17 10:38:00 | 0.4 | 11.94±0.18 |
| *NICER*/XTI | 6203690181 | 2023-07-18 06:38:05 | 2023-07-18 06:39:04 | 0.06 | 12.32±0.48 |
| *Swift*-XRT (PC) | 00016073008 | 2023-07-19 07:34:28 | 2023-07-19 15:46:54 | 1.4 | 0.50±0.01 |
| *Swift*-XRT (PC) | 00016073009 | 2023-07-22 03:40:24 | 2023-07-22 15:01:52 | 0.5 | 0.48±0.03 |
| *NICER*/XTI | 6203690185 | 2023-07-22 17:26:07 | 2023-07-22 20:46:00 | 1.4 | 11.23±0.10 |
| *NICER*/XTI | 6203690186 | 2023-07-23 05:49:09 | 2023-07-23 15:21:00 | 1.7 | 6.45±0.07 |
| *NICER*/XTI | 6203690187 | 2023-07-24 00:23:42 | 2023-07-24 08:23:00 | 1.2 | 4.78±0.07 |
| *Swift*-XRT (PC) | 00016073010‡ | 2023-07-24 22:29:59 | 2023-07-24 22:32:52 | 0.2 | 0.56±0.06 |
| *Swift*-XRT (PC) | 00016073011‡ | 2023-07-25 01:48:54 | 2023-07-25 23:59:54 | 0.5 | 0.54±0.03 |
| *NICER*/XTI | 6203690192 | 2023-07-29 12:10:17 | 2023-07-29 20:02:00 | 2.6 | 17.87±0.09 |
| *Swift*-XRT (PC) | 00016073012 | 2023-07-29 13:43:36 | 2023-07-29 13:46:52 | 0.2 | 0.54±0.05 |
| *NICER*/XTI | 6203690193 | 2023-07-30 09:39:53 | 2023-07-30 14:22:48 | 1.0 | 18.31±0.14 |
| *NICER*/XTI | 6203690195 | 2023-08-01 00:15:48 | 2023-08-01 03:32:01 | 0.9 | 20.55±0.16 |
| *NICER*/XTI | 6203690196 | 2023-08-02 21:16:52 | 2023-08-02 21:20:35 | 0.2 | 20.03±0.31 |
| *Swift*-XRT (PC) | 00016073013 | 2023-08-04 04:09:00 | 2023-08-04 21:59:52 | 1.8 | 0.52±0.02 |
| *Swift*-XRT (PC) | 00016073014 | 2023-08-11 02:29:36 | 2023-08-11 18:36:53 | 1.6 | 0.53±0.02 |
| *NICER*/XTI | 6203690203 | 2023-08-17 09:53:01 | 2023-08-17 11:39:20 | 1.0 | 11.83±0.12 |
| *Swift*-XRT (PC) | 00016073015 | 2023-08-18 02:58:20 | 2023-08-19 23:24:52 | 1.4 | 0.52±0.02 |
| *NICER*/XTI | 6203690204 | 2023-08-18 12:16:27 | 2023-08-18 15:28:20 | 0.7 | 12.99±0.20 |
| *NICER*/XTI | 6203690205 | 2023-08-19 06:49:26 | 2023-08-19 16:24:10 | 2.0 | 13.13±0.13 |
| *NICER*/XTI | 6203690207 | 2023-08-21 03:51:13 | 2023-08-21 03:54:21 | 0.2 | 12.48±0.27 |
| *Swift*-XRT (PC) | 00016073016 | 2023-08-25 02:56:06 | 2023-08-25 09:17:53 | 1.7 | 0.58±0.02 |
| *NICER*/XTI | 6203690209 | 2023-08-26 23:22:35 | 2023-08-26 23:33:00 | 0.6 | 11.56±0.14 |
| *NICER*/XTI | 6203690210 | 2023-08-27 13:20:24 | 2023-08-27 13:29:20 | 0.5 | 11.32±0.15 |
| *NICER*/XTI | 6203690213 | 2023-08-30 09:33:32 | 2023-08-30 09:38:40 | 0.3 | 9.74±0.19 |
| *Swift*-XRT (PC) | 00016073017 | 2023-09-01 07:33:29 | 2023-09-01 07:47:52 | 0.9 | 0.51±0.02 |
| *NICER*/XTI | 6203690215 | 2023-09-01 11:08:55 | 2023-09-01 23:37:20 | 2.5 | 11.83±0.08 |
| *NICER*/XTI | 6203690219 | 2023-09-05 12:38:50 | 2023-09-05 12:45:20 | 0.4 | 11.23±0.18 |
| *NICER*/XTI | 6203690225 | 2023-09-11 23:24:02 | 2023-09-11 23:32:40 | 0.5 | 9.26±0.14 |
| *Swift*-XRT (PC) | 00016073018 | 2023-09-12 10:07:32 | 2023-09-12 13:16:52 | 1.0 | 0.44±0.02 |
| *NICER*/XTI | 6203690226 | 2023-09-12 18:03:08 | 2023-09-12 18:13:26 | 0.4 | 11.05±0.19 |
| *Swift*-XRT (PC) | 00016073019 | 2023-09-18 00:47:05 | 2023-09-18 12:11:52 | 2.1 | 0.46±0.01 |
| *NICER*/XTI | 6203690227 | 2023-09-21 15:49:34 | 2023-09-21 15:53:20 | 0.2 | 7.57±0.20 |
| *NICER*/XTI | 6203690228 | 2023-09-24 13:39:36 | 2023-09-24 16:48:53 | 0.7 | 6.01±0.10 |
| *Swift*-XRT (PC) | 00016073020 | 2023-09-25 20:04:17 | 2023-09-25 23:27:53 | 1.7 | 0.36±0.01 |
| *NICER*/XTI | 6203690229 | 2023-09-29 00:22:34 | 2023-09-29 20:39:40 | 1.5 | 8.27±0.08 |
| *Swift*-XRT (PC) | 00016073021 | 2023-10-02 13:26:23 | 2023-10-02 20:10:53 | 2.1 | 0.46±0.01 |

* The instrumental setup is indicated in brackets: PC = photon counting, WT = windowed timing.
† Count rate in the 0.3–10 keV range for *Swift* and *NICER*, in the 3–60 keV interval for *NuSTAR*. Uncertainties are at $1\sigma$ c.l.
‡ These observations were merged for the spectral analysis.

## Appendix B: Spectral analysis results

Tables B.1 and B.2 report the results of the spectral analysis of the *NICER* spectra, while we listed the best-fitting parameters for the *Swift*-XRT dataset in Table B.3.

**Table B.1.** Best fit values of the single spectra with the black-body component.

| ObsID | $\Gamma$ | $K_{\rm nthc}\times100$ | $kT_{\rm seed}$ (keV) | $kT_{\rm bbody}$ (keV) | $K_{\rm bb}$ | $F_{0510}$ ($\times10^{-10}$ erg cm$^{-2}$ s$^{-1}$) | $\chi^2$ (dof) |
|---|---|---|---|---|---|---|---|
| 6203690102 | 2.01±0.04 | 3.887±0.297 | $0.22^{+0.01}_{-0.01}$ | =kT$_{\rm seed}$ | $1827^{+255}_{-200}$ | 2.34±0.02 | 137(96) |
| 6203690104 | 2.23±0.05 | $4.560^{+0.680}_{-0.435}$ | $0.19^{+0.02}_{-0.04}$ | =kT$_{\rm seed}$ | $1188^{+268}_{-1188}$ | 2.04±0.02 | 74(72) |
| 6203690105 | 1.95±0.04 | 3.280±0.253 | $0.20^{+0.01}_{-0.01}$ | =kT$_{\rm seed}$ | $1768^{+385}_{-266}$ | 1.98±0.01 | 133(98) |
| 6203690106 | $2.17^{+0.04}_{-0.03}$ | 4.430±0.082 | <0.23 | - | - | 1.88±0.02 | 55(66) |
| 6203690110 | 1.84±0.05 | 2.380±0.220 | $0.21^{+0.01}_{-0.01}$ | =kT$_{\rm seed}$ | $1362^{+300}_{-215}$ | 1.67±0.02 | 90(93) |
| 6203690111 | 1.85±0.04 | 2.265±0.203 | $0.19^{+0.02}_{-0.02}$ | =kT$_{\rm seed}$ | $1401^{+526}_{-298}$ | 1.46±0.01 | 116(96) |
| 6203690112 | 1.86±0.06 | 2.012±0.248 | $0.19^{+0.02}_{-0.03}$ | =kT$_{\rm seed}$ | $1171^{+804}_{-330}$ | 1.26±0.02 | 97(83) |
| 6203690113 | 1.93±0.02 | 2.397±0.033 | <0.11 | - | - | 1.22±0.01 | 100(90) |
| 6203690114 | $1.77^{+0.04}_{-0.05}$ | 1.663±0.154 | $0.20^{+0.02}_{-0.02}$ | =kT$_{\rm seed}$ | $866^{+301}_{-179}$ | 1.18±0.01 | 110(97) |
| 6203690116 | 1.66±0.05 | 1.183±0.117 | $0.20^{+0.02}_{-0.02}$ | =kT$_{\rm seed}$ | $618^{+312}_{-160}$ | 0.93±0.01 | 108(96) |
| 6203690119 | 1.66±0.04 | 1.023±0.031 | <0.12 | - | - | 0.68±0.02 | 120(80) |
| 6203690120 | 1.70±0.03 | 0.994±0.013 | <0.13 | - | - | 0.64±0.01 | 110(89) |
| 6203690122 | 1.71±0.04 | 0.920±0.031 | <0.13 | - | - | 0.58±0.01 | 88(78) |
| 6203690123 | $1.66^{+0.09}_{-0.07}$ | 0.765±0.027 | <0.24 | - | - | 0.51±0.02 | 61(56) |
| 6203690124 | $1.45^{+0.05}_{-0.04}$ | 0.517±0.021 | <0.15 | - | - | 0.44±0.01 | 79(83) |
| 6203690130 | $1.39^{+0.09}_{-0.07}$ | 0.269±0.027 | <0.40 | - | - | 0.26±0.01 | 57(74) |
| 6203690131 | $1.49^{+0.07}_{-0.06}$ | 0.307±0.029 | $0.22^{+0.06}_{-0.22}$ | - | - | 0.27±0.01 | 77(84) |
| 6203690134 | $1.58^{+0.12}_{-0.09}$ | 0.368±0.030 | <0.37 | - | - | 0.28±0.01 | 56(59) |
| 6203690135 | $1.34^{+0.04}_{-0.03}$ | 0.272±0.009 | <0.19 | - | - | 0.27±0.01 | 78(88) |
| 6203690136 | $1.40^{+0.06}_{-0.05}$ | 0.286±0.021 | <0.36 | - | - | 0.27±0.01 | 70(85) |
| 6203690137 | 1.40±0.04 | 0.279±0.010 | <0.19 | - | - | 0.26±0.01 | 58(80) |
| 6203690138 | $1.32^{+0.06}_{-0.07}$ | 0.272±0.015 | <0.18 | - | - | 0.28±0.01 | 49(62) |
| 6203690139 | $1.28^{+0.07}_{-0.06}$ | 0.306±0.020 | <0.22 | - | - | 0.33±0.02 | 73(71) |
| 6203690140 | $1.39^{+0.09}_{-0.08}$ | 0.313±0.020 | <0.17 | - | - | 0.29±0.02 | 63(57) |
| 6203690145 | $1.33^{+0.06}_{-0.05}$ | 0.217±0.014 | <0.22 | - | - | 0.22±0.01 | 65(73) |
| 6203690149 | $1.87^{+0.74}_{-0.35}$ | 0.117±0.030 | $0.36^{+0.15}_{-0.18}$ | - | - | 0.10±0.01 | 52(52) |
| 6203690151 | $1.00^{+0.17}_{-1.00}$ | 0.063±0.021 | <0.74 | - | - | 0.14±0.01 | 57(58) |
| 6203690152 | $1.00^{+0.07}_{-1.00}$ | 0.093±0.007 | <0.27 | - | - | 0.16±0.01 | 48(57) |
| 6203690157 | $1.96^{+0.03}_{-0.02}$ | 1.748±0.028 | <0.11 | - | - | 0.87±0.01 | 119(90) |
| 6203690159 | 1.78±0.09 | 1.354±0.220 | $0.23^{+0.02}_{-0.02}$ | =kT$_{\rm seed}$ | $654^{+243}_{-145}$ | 1.03±0.02 | 96(88) |
| 6203690160 | $1.95^{+0.05}_{-0.04}$ | 1.951±0.061 | <0.22 | - | - | 0.97±0.02 | 111(79) |
| 6203690162 | $1.80^{+0.09}_{-0.10}$ | 1.382±0.247 | $0.21^{+0.02}_{-0.03}$ | =kT$_{\rm seed}$ | $745^{+443}_{-216}$ | 0.99±0.02 | 83(81) |
| 6203690163 | 1.76±0.06 | 1.358±0.140 | $0.21^{+0.02}_{-0.02}$ | =kT$_{\rm seed}$ | $877^{+287}_{-181}$ | 1.01±0.01 | 93(87) |

**Table B.1.** Continued.

| ObsID | Γ | $K_{\rm nthc}\times100$ | $kT_{\rm seed}$ (keV) | $kT_{\rm bbody}$ (keV) | $K_{\rm bb}$ | $F_{0510}$ ($\times10^{-10}$ erg cm$^{-2}$ s$^{-1}$) | $\chi^2$ (dof) |
|---|---|---|---|---|---|---|---|
| 6203690165 | $1.69^{+0.09}_{-0.10}$ | 1.517±0.224 | $0.20^{+0.02}_{-0.02}$ | =kT$_{\rm seed}$ | $1484^{+1013}_{-485}$ | 1.21±0.03 | 55(79) |
| 6203690166 | 1.79±0.07 | 1.417±0.195 | $0.22^{+0.02}_{-0.02}$ | =kT$_{\rm seed}$ | $793^{+311}_{-178}$ | 1.04±0.01 | 110(88) |
| 6203690169 | $1.77^{+0.08}_{-0.09}$ | 1.176±0.199 | $0.21^{+0.02}_{-0.03}$ | =kT$_{\rm seed}$ | $598^{+327}_{-163}$ | 0.86±0.02 | 88(87) |
| 6203690170 | 1.81±0.08 | 1.263±0.183 | $0.21^{+0.02}_{-0.02}$ | =kT$_{\rm seed}$ | $788^{+363}_{-198}$ | 0.91±0.02 | 120(88) |
| 6203690171 | 1.93±0.03 | 1.591±0.040 | <0.13 | - | - | 0.81±0.01 | 92(88) |
| 6203690172 | $1.87^{+0.06}_{-0.05}$ | 1.627±0.072 | <0.15 | - | - | 0.88±0.03 | 95(77) |
| 6203690173 | 1.89±0.04 | 1.359±0.173 | <0.13 | - | - | 0.72±0.01 | 86(86) |
| 6203690179 | $1.97^{+0.12}_{-0.10}$ | 1.299±0.098 | <0.34 | - | - | 0.65±0.03 | 102(73) |
| 6203690180 | $1.18^{+0.10}_{-0.12}$ | 0.716±0.114 | $0.17^{+0.04}_{-0.04}$ | =kT$_{\rm seed}$ | $1814^{+6148}_{-1217}$ | 1.02±0.04 | 106(80) |
| 6203690181 | $1.99^{+0.43}_{-0.27}$ | 1.235±0.234 | <0.44 | - | - | 0.66±0.07 | 62(47) |
| 6203690185 | 1.80±0.03 | 1.270±0.030 | <0.14 | - | - | 0.73±0.01 | 110(88) |
| 6203690186 | 1.72±0.09 | 1.006±0.165 | $0.21^{+0.03}_{-0.03}$ | =kT$_{\rm seed}$ | $565^{+370}_{-176}$ | 0.77±0.02 | 77(86) |
| 6203690187 | 1.83±0.05 | 1.324±0.048 | <0.16 | - | - | 0.74±0.02 | 73(79) |
| 6203690192 | 1.79±0.05 | 1.548±0.149 | $0.21^{+0.01}_{-0.02}$ | =kT$_{\rm seed}$ | $1035^{+317}_{-204}$ | 1.12±0.01 | 108(95) |
| 6203690193 | 1.81±0.07 | 1.672±0.210 | $0.20^{+0.02}_{-0.02}$ | =kT$_{\rm seed}$ | $1187^{+655}_{-334}$ | 1.15±0.02 | 71(88) |
| 6203690195 | $1.89^{+0.08}_{-0.09}$ | 1.775±0.262 | $0.22^{+0.02}_{-0.02}$ | =kT$_{\rm seed}$ | $1119^{+363}_{-232}$ | 1.23±0.02 | 92(87) |
| 6203690196 | $1.64^{+0.14}_{-0.16}$ | 1.590±0.387 | $0.19^{+0.04}_{-0.04}$ | =kT$_{\rm seed}$ | $1693^{+3531}_{-811}$ | 1.33±0.05 | 72(77) |
| 6203690203 | $1.81^{+0.10}_{-0.12}$ | 1.154±0.249 | $0.22^{+0.03}_{-0.04}$ | =kT$_{\rm seed}$ | $554^{+400}_{-167}$ | 0.82±0.02 | 61(78) |
| 6203690204 | $2.08^{+0.08}_{-0.06}$ | 1.768±0.052 | <0.18 | - | - | 0.79±0.02 | 45(65) |
| 6203690205 | $1.42^{+0.15}_{-0.16}$ | 0.734±0.160 | $0.24^{+0.02}_{-0.02}$ | =kT$_{\rm seed}$ | $511^{+175}_{-112}$ | 0.89±0.02 | 36(68) |
| 6203690207 | 2.09±0.08 | 1.659±0.093 | <0.14 | - | - | 0.74±0.03 | 72(72) |
| 6203690209 | 2.05±0.04 | 1.530±0.050 | <0.14 | - | - | 0.71±0.02 | 88(81) |
| 6203690210 | $1.97^{+0.06}_{-0.05}$ | 1.434±0.044 | <0.20 | - | - | 0.70±0.02 | 55(79) |
| 6203690213 | 2.01±0.07 | 1.238±0.059 | <0.16 | - | - | 0.59±0.02 | 90(74) |
| 6203690215 | $1.72^{+0.06}_{-0.07}$ | 0.982±0.120 | $0.21^{+0.02}_{-0.02}$ | =kT$_{\rm seed}$ | $581^{+255}_{-142}$ | 0.76±0.01 | 107(90) |
| 6203690219 | 2.04±0.06 | 1.446±0.067 | <0.23 | - | - | 0.67±0.02 | 89(77) |
| 6203690225 | 2.01±0.06 | 1.186±0.045 | <0.14 | - | - | 0.57±0.02 | 84(77) |
| 6203690226 | 1.68±0.07 | 1.086±0.057 | <0.13 | - | - | 0.71±0.03 | 144(79) |
| 6203690227 | $1.73^{+0.10}_{-0.09}$ | 0.869±0.064 | <0.16 | - | - | 0.54±0.03 | 52(72) |
| 6203690228 | 1.71±0.06 | 0.627±0.030 | <0.15 | - | - | 0.40±0.01 | 89(78) |
| 6203690229 | $1.92^{+0.04}_{-0.03}$ | 1.015±0.028 | <0.13 | - | - | 0.52±0.01 | 77(88) |

**Notes.** The results derive from the modelling of the single *NICER* spectra using Model 0 or Model 1A, according to the statistical significance of the fit in each case. $K_{\rm nthc}$ and $K_{\rm bb}$ are the normalisations of the `nthcomp` and `bbodyrad` components, respectively. The unabsorbed flux is estimated in the 0.5–10 keV energy interval.

**Table B.2.** Best fit values of the single spectra with the disc component.

| ObsID | Γ | $K_{\rm nthc}\times100$ | $kT_{\rm seed}$ (keV) | $kT_{\rm disk}$ (keV) | $K_{\rm disk}$ | $F_{0510}$ ($\times10^{-10}$ erg cm$^{-2}$ s$^{-1}$) | $\chi^2$ (dof) |
|---|---|---|---|---|---|---|---|
| 6203690102 | 1.93±0.05 | 3.501±0.310 | $0.34^{+0.02}_{-0.02}$ | $=kT_{\rm seed}$ | $258^{+46}_{-35}$ | 2.41±0.02 | 109(96) |
| 6203690104 | $2.19^{+0.07}_{-0.08}$ | 4.153±0.564 | $0.31^{+0.03}_{-0.04}$ | $=kT_{\rm seed}$ | $188^{+40}_{-39}$ | 2.08±0.02 | 72(72) |
| 6203690105 | 1.88±0.05 | 3.016±0.270 | $0.31^{+0.02}_{-0.02}$ | $=kT_{\rm seed}$ | $253^{+68}_{-47}$ | 2.02±0.01 | 114(98) |
| 6203690106 | $2.09^{+0.09}_{-0.12}$ | 3.565±0.812 | $0.27^{+0.05}_{-0.10}$ | $=kT_{\rm seed}$ | $307^{+324}_{-72}$ | 1.84±0.03 | 52(65) |
| 6203690110 | 1.77±0.07 | 2.204±0.247 | $0.33^{+0.02}_{-0.03}$ | $=kT_{\rm seed}$ | $202^{+61}_{-42}$ | 1.72±0.02 | 79(93) |
| 6203690111 | 1.80±0.06 | 2.115±0.217 | $0.30^{+0.03}_{-0.03}$ | $=kT_{\rm seed}$ | $201^{+92}_{-52}$ | 1.49±0.01 | 104(96) |
| 6203690112 | $1.80^{+0.08}_{-0.09}$ | 1.852±0.271 | $0.30^{+0.04}_{-0.05}$ | $=kT_{\rm seed}$ | $159^{+121}_{-52}$ | 1.28±0.02 | 92(83) |
| 6203690113 | $1.82^{+0.08}_{-0.09}$ | 1.893±0.328 | $0.28^{+0.05}_{-0.08}$ | $=kT_{\rm seed}$ | $163^{+403}_{-68}$ | 1.24±0.02 | 92(89) |
| 6203690114 | 1.71±0.06 | 1.563±0.168 | $0.32^{+0.03}_{-0.03}$ | $=kT_{\rm seed}$ | $119^{+54}_{-31}$ | 1.21±0.01 | 100(97) |
| 6203690116 | 1.62±0.06 | 1.159±0.125 | $0.30^{+0.04}_{-0.04}$ | $=kT_{\rm seed}$ | $94^{+70}_{-32}$ | 0.95±0.01 | 103(96) |
| 6203690119 | $1.51^{+0.09}_{-0.14}$ | 0.826±0.119 | $0.25^{+0.10}_{-0.08}$ | $=kT_{\rm seed}$ | $148^{+1018}_{-106}$ | 0.73±0.02 | 102(79) |
| 6203690120 | 1.70±0.03 | 0.994±0.026 | <0.18 | - | - | 0.64±0.01 | 110(89) |
| 6203690122 | 1.71±0.04 | 0.921±0.028 | <0.20 | - | - | 0.58±0.01 | 88(78) |
| 6203690123 | $1.65^{+0.10}_{-0.07}$ | 0.765±0.036 | <0.34 | - | - | 0.51±0.02 | 61(56) |
| 6203690124 | $1.26^{+0.14}_{-0.20}$ | 0.375±0.104 | $0.34^{+0.15}_{-0.17}$ | $=kT_{\rm seed}$ | $21^{+456}_{-15}$ | 0.47±0.02 | 67(82) |
| 6203690130 | $1.41^{+0.14}_{-0.08}$ | 0.269±0.024 | <0.80 | - | - | 0.26±0.01 | 57(74) |
| 6203690131 | $1.52^{+0.12}_{-0.08}$ | 0.307±0.022 | $0.43^{+0.18}_{-0.22}$ | - | - | 0.27±0.01 | 75(84) |
| 6203690134 | $1.64^{+0.24}_{-0.13}$ | 0.359±0.037 | <0.79 | - | - | 0.27±0.01 | 55(59) |
| 6203690135 | 1.34±0.04 | 0.272±0.007 | <0.38 | - | - | 0.27±0.01 | 78(88) |
| 6203690136 | $1.41^{+0.08}_{-0.06}$ | 0.288±0.009 | <0.60 | - | - | 0.27±0.01 | 70(85) |
| 6203690137 | 1.40±0.04 | 0.279±0.009 | <0.34 | - | - | 0.26±0.01 | 58(80) |
| 6203690138 | 1.32±0.06 | 0.272±0.015 | <0.35 | - | - | 0.28±0.01 | 49(62) |
| 6203690139 | 1.29±0.07 | 0.306±0.019 | <0.47 | - | - | 0.33±0.02 | 73(71) |
| 6203690140 | $1.39^{+0.09}_{-0.08}$ | 0.312±0.022 | <0.31 | - | - | 0.29±0.02 | 63(57) |
| 6203690145 | $1.33^{+0.06}_{-0.05}$ | 0.217±0.011 | <0.44 | - | - | 0.22±0.01 | 65(73) |
| 6203690149 | <1.70 | 0.121±0.017 | <2.20 | - | - | 0.09±0.01 | 48(52) |
| 6203690151 | <1.03 | 0.067±0.009 | <2.41 | - | - | 0.14±0.01 | 54(58) |
| 6203690152 | <1.07 | 0.093±0.007 | <1.10 | - | - | 0.16±0.01 | 48(57) |
| 6203690157 | 1.96±0.02 | 1.750±0.035 | <0.15 | - | - | 0.87±0.01 | 119(90) |
| 6203690159 | $1.71^{+0.11}_{-0.13}$ | 1.282±0.251 | $0.35^{+0.04}_{-0.05}$ | $=kT_{\rm seed}$ | $97^{+54}_{-29}$ | 1.06±0.02 | 93(88) |
| 6203690160 | $1.95^{+0.05}_{-0.04}$ | 1.951±0.062 | <0.28 | - | - | 0.97±0.02 | 111(79) |
| 6203690162 | $1.75^{+0.12}_{-0.14}$ | 1.333±0.284 | $0.32^{+0.05}_{-0.06}$ | $=kT_{\rm seed}$ | $114^{+110}_{-44}$ | 1.01±0.02 | 83(81) |
| 6203690163 | $1.67^{+0.08}_{-0.09}$ | 1.234±0.165 | $0.32^{+0.03}_{-0.03}$ | $=kT_{\rm seed}$ | $125^{+56}_{-33}$ | 1.04±0.01 | 84(87) |
| 6203690165 | $1.64^{+0.11}_{-0.13}$ | 1.475±0.260 | $0.28^{+0.05}_{-0.05}$ | $=kT_{\rm seed}$ | $284^{+327}_{-126}$ | 1.24±0.03 | 55(79) |
| 6203690166 | $1.70^{+0.10}_{-0.11}$ | 1.270±0.215 | $0.34^{+0.04}_{-0.04}$ | $=kT_{\rm seed}$ | $109^{+55}_{-31}$ | 1.07±0.02 | 101(88) |
| 6203690169 | $1.71^{+0.11}_{-0.13}$ | 1.098±0.221 | $0.33^{+0.05}_{-0.06}$ | $=kT_{\rm seed}$ | $84^{+65}_{-29}$ | 0.88±0.02 | 85(87) |

**Table B.2.** Continued.

| ObsID | Γ | $K_{\rm nthc}\times100$ | $kT_{\rm seed}$ (keV) | $kT_{\rm disk}$ (keV) | $K_{\rm disk}$ | $F_{0510}$ ($\times10^{-10}$ erg cm$^{-2}$ s$^{-1}$) | $\chi^2$ (dof) |
|---|---|---|---|---|---|---|---|
| 6203690170 | $1.76^{+0.09}_{-0.10}$ | 1.221±0.200 | $0.31^{+0.04}_{-0.04}$ | $=kT_{\rm seed}$ | $131^{+89}_{-44}$ | 0.93±0.02 | 117(88) |
| 6203690171 | 1.93±0.03 | 1.592±0.040 | $0.01^{+0.18}_{-0.01}$ | - | - | 0.81±0.01 | 92(88) |
| 6203690172 | $1.87^{+0.06}_{-0.05}$ | 1.626±0.053 | <0.22 | - | - | 0.88±0.03 | 95(77) |
| 6203690173 | 1.89±0.04 | 1.360±0.041 | <0.19 | - | - | 0.72±0.01 | 86(86) |
| 6203690179 | $1.97^{+0.14}_{-0.10}$ | 1.307±0.094 | <0.50 | - | - | 0.66±0.03 | 102(73) |
| 6203690180 | $1.11^{+0.14}_{-1.11}$ | 0.656±0.145 | $0.26^{+0.08}_{-0.08}$ | $=kT_{\rm seed}$ | $257^{+1273}_{-210}$ | 1.02±0.04 | 104(80) |
| 6203690181 | $2.06^{+1.16}_{-0.32}$ | 1.240±0.230 | <0.79 | - | - | 0.66±0.07 | 61(47) |
| 6203690185 | 1.80±0.03 | 1.270±0.030 | <0.20 | - | - | 0.73±0.01 | 110(88) |
| 6203690186 | $1.68^{+0.11}_{-0.13}$ | 0.996±0.190 | $0.31^{+0.06}_{-0.06}$ | $=kT_{\rm seed}$ | $92^{+108}_{-40}$ | 0.79±0.02 | 78(86) |
| 6203690187 | 1.83±0.05 | 1.324±0.129 | <0.25 | - | - | 0.74±0.02 | 73(79) |
| 6203690192 | 1.72±0.07 | 1.438±0.165 | $0.32^{+0.03}_{-0.03}$ | $=kT_{\rm seed}$ | $157^{+64}_{-39}$ | 1.15±0.01 | 97(95) |
| 6203690193 | $1.77^{+0.08}_{-0.10}$ | 1.632±0.244 | $0.29^{+0.04}_{-0.05}$ | $=kT_{\rm seed}$ | $205^{+187}_{-79}$ | 1.17±0.02 | 70(88) |
| 6203690195 | $1.82^{+0.11}_{-0.12}$ | 1.660±0.306 | $0.33^{+0.04}_{-0.04}$ | $=kT_{\rm seed}$ | $178^{+87}_{-50}$ | 1.27±0.02 | 90(87) |
| 6203690196 | $1.57^{+0.18}_{-0.23}$ | 1.481±0.453 | $0.29^{+0.08}_{-0.09}$ | $=kT_{\rm seed}$ | $279^{+1016}_{-170}$ | 1.36±0.05 | 71(77) |
| 6203690203 | $1.76^{+0.13}_{-0.16}$ | 1.120±0.272 | $0.32^{+0.06}_{-0.07}$ | $=kT_{\rm seed}$ | $87^{+98}_{-35}$ | 0.84±0.02 | 59(78) |
| 6203690204 | $2.08^{+0.08}_{-0.06}$ | 1.767±0.062 | <0.24 | - | - | 0.79±0.02 | 45(65) |
| 6203690207 | $2.08^{+0.08}_{-0.07}$ | 1.655±0.094 | <0.20 | - | - | 0.74±0.03 | 72(72) |
| 6203690209 | $2.05^{+0.05}_{-0.04}$ | 1.530±0.059 | <0.20 | - | - | 0.71±0.02 | 88(81) |
| 6203690210 | $1.97^{+0.06}_{-0.05}$ | 1.434±0.050 | <0.25 | - | - | 0.70±0.02 | 56(79) |
| 6203690213 | 2.01±0.07 | 1.238±0.040 | <0.23 | - | - | 0.59±0.02 | 90(74) |
| 6203690215 | $1.64^{+0.09}_{-0.10}$ | 0.900±0.138 | $0.33^{+0.04}_{-0.04}$ | $=kT_{\rm seed}$ | $80^{+49}_{-25}$ | 0.78±0.01 | 100(90) |
| 6203690219 | $2.04^{+0.09}_{-0.07}$ | 1.441±0.071 | <0.35 | - | - | 0.67±0.02 | 89(77) |
| 6203690225 | $2.00^{+0.06}_{-0.05}$ | 1.185±0.052 | <0.20 | - | - | 0.57±0.02 | 84(77) |
| 6203690226 | $1.25^{+0.23}_{-1.25}$ | 0.605±0.288 | $0.31^{+0.12}_{-0.11}$ | $=kT_{\rm seed}$ | $107^{+681}_{-78}$ | 0.83±0.04 | 118(78) |
| 6203690227 | $1.74^{+0.09}_{-0.10}$ | 0.872±0.101 | <0.26 | - | - | 0.54±0.03 | 52(72) |
| 6203690228 | 1.71±0.06 | 0.627±0.016 | <0.25 | - | - | 0.40±0.01 | 89(78) |
| 6203690229 | $1.92^{+0.03}_{-0.04}$ | 1.016±0.030 | <0.18 | - | - | 0.52±0.01 | 77(88) |

**Notes.** The results derive from the modelling of the single *NICER* spectra using Model 0 or Model 1B, according to the statistical significance of the fit in each case. $K_{\rm nthc}$ and $K_{\rm disc}$ are the normalisations of the `nthcomp` and `diskbb` components, respectively. The unabsorbed flux is estimated in the 0.5–10 keV energy interval.

**Table B.3.** Best fit values of the *Swift* spectra.

| Obs. | $\Gamma$ | $K_{\rm nthc}$ ($\times100$) | $F_{0510}$ ($\times10^{-11}$ erg cm$^{-2}$ s$^{-1}$) | $\chi^2$ (dof) |
|---|---|---|---|---|
| 1 | 1.83±0.05 | 6.53±0.29 | 36±1 | 41.42(48) |
| 2 | 2.13±0.05 | 5.01±0.24 | 21.5±0.4 | 161.75(145) |
| 3 | 1.97±0.06 | 3.02±0.18 | 14.7±0.4 | 83.56(86) |
| 4 | 2.07±0.05 | 3.57±0.18 | 16.1±0.3 | 141.22(130) |
| 5 | 1.88±0.06 | 1.76±0.12 | 9.3±0.3 | 93.61(79) |
| 6 | 1.78±0.06 | 1.33±0.09 | 7.8±0.3 | 68.45(65) |
| 7 | 1.72±0.10 | 0.92±0.10 | 5.7±0.3 | 44.18(27) |
| 8 | 1.73±0.11 | 0.77±0.09 | 4.7±0.3 | 29.93(30) |
| 9 | 1.55±0.14 | 0.64±0.10 | 4.8±0.4 | 4.62(14) |
| 10 | 1.45±0.14 | 0.47±0.07 | 3.9±0.3 | 16.08(15) |
| 11 | 1.24±0.18 | 0.25±0.05 | 2.9±0.4 | 8.06(13) |
| 12 | 1.32±0.09 | 0.34±0.04 | 3.4±0.2 | 32.16(29) |
| 13 | <1.11 | $0.17^{+0.03}_{-0.01}$ | 2.9±0.3 | 5.28(10) |
| 14 | 1.20±0.11 | 0.21±0.03 | 2.5±0.2 | 16.97(18) |
| 15 | 1.36±0.13 | 0.26±0.04 | 2.5±0.2 | 12.71(18) |
| 16 | 1.35±0.16 | 0.22±0.03 | 2.1±0.2 | 19.44(20) |
| 16 | 1.24±0.14 | 0.16±0.01 | 1.8±0.2 | 14.09(21) |
| 18 | <1.41 | 0.05±0.01 | 0.6±0.1 | 5.31(12) |
| 19 | <1.22 | 0.04±0.01 | $0.6^{\pm}0.1$ | 9.60(10) |
| 20 | <1.28 | 0.07±0.02 | 1.1±0.2 | 13.99(14) |
| 21 | 1.46±0.14 | 0.27±0.04 | 2.3±0.2 | 36.73(42) |
| 22 | 1.75±0.13 | 0.83±0.11 | 5.0±0.4 | 63.02(64) |
| 23 | 1.75±0.13 | 1.49±0.19 | 9.0±0.6 | 50.03(57) |
| 24 | 1.69±0.15 | 1.29±0.20 | 8.3±0.7 | 24.58(40) |
| 25 | 1.69±0.16 | 1.57±0.25 | 10±1 | 25.80(36) |
| 26 | 1.89±0.18 | 1.81±0.30 | 9±1 | 24.37(34) |
| 27 | 1.50±0.17 | 0.82±0.16 | 6.6±0.8 | 25.17(25) |
| 28 | 1.59±0.12 | 0.69±0.09 | 4.9±0.4 | 63.87(62) |
| 29 | 1.54±0.20 | 0.61±0.13 | 4.6±0.6 | 18.23(21) |
| 30 | 1.86±0.19 | 1.14±0.21 | 6.1±0.6 | 40.38(30) |
| 31 | 1.91±1.36 | $2.21^{+0.70}_{-0.63}$ | 11±2 | 6.11(8) |
| 32 | 1.76±0.10 | 1.39±0.15 | 8.3±0.5 | 77.04(87) |
| 33 | 1.82±0.11 | 1.48±0.17 | 8.3±0.5 | 57.25(75) |
| 34 | 1.83±0.12 | 1.07±0.13 | 5.9±0.4 | 52.77(62) |
| 35 | 1.84±0.11 | 0.95±0.10 | 5.3±0.3 | 97.30(83) |
| 36 | 1.94±0.15 | 1.24±0.18 | 6.3±0.5 | 38.69(40) |
| 37 | 1.78±0.16 | 0.71±0.11 | 4.2±0.4 | 33.20(39) |
| 38 | 1.86±0.10 | 0.89±0.09 | 4.8±0.3 | 62.00(85) |
| 39 | 1.58±0.13 | 0.49±0.06 | 3.5±0.3 | 34.67(54) |
| 40 | 1.77±0.11 | 0.68±0.07 | 4.0±0.2 | 77.90(84) |

**Notes.** The results derive from simultaneously modelling the *Swift*-XRT spectra using Model 0. The $N_{\rm H}$ was frozen to $0.9\times10^{22}$ cm$^{-2}$. $K_{\rm nthc}$ is the normalisation of the `nthcomp` component. In the fit, the $kT_{\rm seed}$ parameter was fixed to 0.1 keV. The flux is unabsorbed and in the 0.5–10 keV energy interval.